

Article

Temperature-Dependent FTIRS Study of Manganese Oxide Spinel Obtained by Solution Combustion Synthesis (SCS) for Supercapacitor Applications

Taylan Karakoç, Sécou Sall and Sergey N. Pronkin * 

Institute of Chemistry and Processes for Energy, Environment and Health (ICPEES), UMR-7515, 25 Rue Becquerel, CEDEX 2, 67087 Strasbourg, France; taylan.karakoc@etu.unistra.fr (T.K.); ssall@unistra.fr (S.S.)

* Correspondence: sergey.pronkin@unistra.fr; Tel.: +33-3-68-85-28-53

Abstract: Solution combustion synthesis (SCS) is often utilized to prepare crystalline nanoparticles of transition metal oxides, in particular Mn oxides. The structure and composition of the final product depend on the conditions of the synthesis, in particular on the composition of metal precursors, its molar ratio to the fuel component, and the mode of heating. In the present work, the study of chemical phenomena that may occur in the SCS process has been studied for the conventional nitrate–glycine synthesis of Mn oxide, as well as for nitrate–citrate–glycine and nitrate–citrate–urea synthesis. In the case of nitrate–glycine synthesis at a 1:1 fuel-to-salt ratio, the formation of a weak complex of Mn(II) and glycine provides the conditions for an instantaneous SCS reaction upon heating, resulting in slight sintering of final oxide nanoparticles. Partial hydrolysis of the Mn precursor during slow solvent evaporation results in the formation of a mixture of oxides, namely MnO and Mn₃O₄. Formation of MnO is completely suppressed when ammonium citrate is added into the initial mixture. Pure Mn₂O₃ oxide is obtained from nitrate–citrate synthesis, while the pure Mn₃O₄ phase is obtained in the case of nitrate–citrate–glycine and nitrate–citrate–urea synthesis, due to the higher temperature generated in the presence of additional fuel. In the presence of citrate, the SCS reaction is slower, resulting in stronger sintering of the nanoparticles. The study of the electrochemical properties of synthesized oxides demonstrates that SCS with the nitrate–citrate–urea mixture provides the highest charge capacitance in 1 M NaOH: 130 F/g at 2 A/g. The impedance characterization of materials allows us to propose a tentative mechanism of degradation of electrode materials during galvanostatic cycling.

Keywords: solution combustion synthesis; manganese oxide; hausmannite; DRIFTS; supercapacitor



Academic Editor: Carmen Lăzău

Received: 23 September 2024

Revised: 25 October 2024

Accepted: 29 October 2024

Published: 21 January 2025

Citation: Karakoç, T.; Sall, S.; Pronkin, S.N. Temperature-Dependent FTIRS Study of Manganese Oxide Spinel Obtained by Solution Combustion Synthesis (SCS) for Supercapacitor Applications. *Batteries* **2025**, *11*, 39. <https://doi.org/10.3390/batteries11020039>

Copyright: © 2025 by the authors. Licensee MDPI, Basel, Switzerland. This article is an open access article distributed under the terms and conditions of the Creative Commons Attribution (CC BY) license (<https://creativecommons.org/licenses/by/4.0/>).

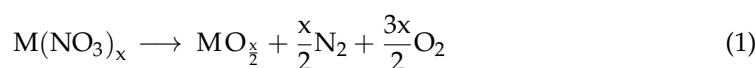
1. Introduction

Transition metal oxides (TMOs) are one of the main classes of materials used as electrodes in electrochemical energy storage devices (EESDs), in particular in batteries [1,2] and pseudocapacitors [3]. Manganese oxides are historically among the most studied electrode materials for EESDs [1,4,5]. In particular, spinel manganese oxide (Mn₃O₄) has been intensively studied in recent years as a promising electrode material for pseudocapacitors [6–8] and anodes of Li-ion batteries [9,10]. The electrochemical properties of manganese oxides can be adjusted by tuning their composition, by partially or totally replacing one of the cations [5]. Dosaev et al. [11] prepared a series of AMn₂O₄ substituted spinels with A = Li, Mg, and Cd, thus controllably varying unit cell parameters and the oxidation state of Mn

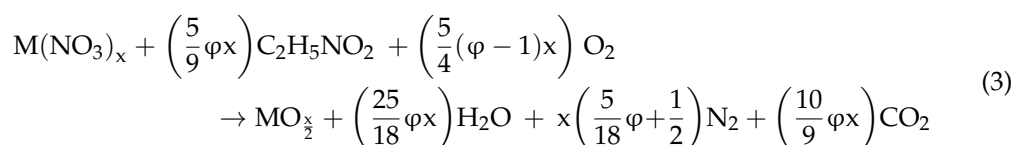
from +2.5 (in Mn_3O_4) to +3.5 (in LiMn_2O_4). They observed a systematic dependence of the electrocatalytic activity of prepared oxides on the oxidation state of Mn.

Solution combustion synthesis (SCS) has been known for decades as a low-cost, low-energy intake and versatile method of preparation of binary and mixed oxides [12,13], such as aluminates [14], chromates [15], and manganates [16]. The method allows preparation of well-crystallized mesoporous oxide powders, consisting of particles within the size range of a few tens nm to a few μm . In SCS, the metal precursor salt, which is most commonly a nitrate, is dissolved in a solution with the fuel component, the most common being glycine, urea, sucrose, or citric acid [17]. The solvent is then evaporated until the fuel is ignited at a relatively low temperature (100–200 °C), generating heat and resulting in fast decomposition of the metal salt. The self-propagating character of the process ensures a relatively short reaction time and uniform conditions of the reaction. Decomposition of both nitrates and fuels results in the formation of a large number of gaseous products, allowing the heat to be rapidly dissipated, minimizing sintering of solid products.

The main challenge of SCS is to ensure control of the morphology and composition of the resulting oxide materials due to the complexity of the processes occurring during the synthesis in a short reaction time. In the most common version of SCS, the nitrate and glycine are used as precursor and fuel, correspondingly, and the stoichiometric reactions of their decomposition are often expressed as the simple reactions in Equations (1) and (2).



The overall stoichiometric equation for the mixture containing glycine and nitrate in the molar ratio of φ is given by Equation (3).



The above equations are often used for categorizing the composition of the initial system as fuel-lean ($\varphi < 1$) or fuel-rich ($\varphi > 1$) mixtures. In particular, when $\varphi = 1$, the amount of oxygen consumed by glycine combustion is supposed to be equivalent to the amount of oxygen produced by nitrate decomposition. In this case, no oxygen depletion is expected in the reaction media despite the escape of a large number of hot gaseous products of decomposition.

However, it is also well recognized that reactions (1) and (2) are oversimplifications of the complex mechanism of decomposition reactions occurring at the high temperature of SCS synthesis. Some of the reactions that may occur during the SCS process with $\text{Mn}(\text{NO}_3)_2$ are given in Table S1 in the Supporting Information section. The latter does not list all possible reactions and processes occurring during SCS. In particular, formation of metal complexes with fuel components, for example complexes of Mn with glycine [18], may occur during the evaporation of solvent, and result in change in the ignition and adiabatic temperatures for the SCS process. The intermediate and final products of decomposition reactions may undergo phase transitions, also resulting in changes in reaction heat.

In numerous studies, the analysis of the thermodynamic effects of the SCS reaction is performed by calculating the adiabatic temperature (T_{ad}) from the energy balance equation, taking into account enthalpies of decomposition reactions and phase transitions, and heat loss due to the escape of hot gaseous products [17,19]. This analysis gives valuable qualitative predictions of the dependence of T_{ad} on the composition of the initial SCS mixture.

However, the maximal temperature detected in the SCS process (T_{\max}) is systematically higher than the predicted T_{ad} values due to (i) uncertainty in the thermodynamic parameters of reagents and intermediates of SCS processes and (ii) limitations in modelling of heat dissipation during fast SCS reactions. In order to better understand the nature of SCS processes and being able to adjust the conditions to synthesize the materials with the desired structure and composition, a combination of thermodynamic analysis and detailed experimental studies is necessary.

Table S2 (Supporting Information) summarizes recent studies of SCS synthesis of Mn oxides. From this table it is clear that the composition and the structure of the final oxide product strongly depends on the conditions of SCS. Namely, the determining composition parameters are the composition of the initial mixture, heating ramp, duration, and temperature. However, the effect of these parameters on the composition and structure of the final products is not yet understood.

The goal of the present work is to understand better the processes occurring during SCS synthesis, how they can be controlled, and how they influence the structure of the resulting oxides, as well as their electrochemical properties as supercapacitor electrode materials. For this, we have performed FTIR characterization of various dried precursors and their mixtures, as well as a temperature-dependent FTIR study of their decomposition. Finally, we have tested the electrochemical properties of the formed oxides and evaluated their performance as electrodes for supercapacitors.

2. Materials and Methods

2.1. Synthesis of Mn Oxides

Different syntheses of manganese oxides were performed by varying the fuel-to-precursor ratio as well as the addition or not of a ligand, as listed in Table 1. The nitrogen adsorption–desorption isotherms of the compounds are presented in the Supplementary Information.

Table 1. Composition of initial mixtures. ($\text{Mn}(\text{NO}_3)_2 \cdot 4\text{H}_2\text{O}$ was used as a metal precursor salt in all syntheses).

Name	Fuel	XRD Attribution	Properties
MnO _x -NG-0.5	Glycine, $\varphi = 0.50$	Mn ₂ O ₃ + [Mn ₃ O ₄] ¹	23–26 nm ² , 17 m ² /g
MnO _x -NG-0.75	Glycine, $\varphi = 0.75$	Mn ₂ O ₃ + Mn ₃ O ₄	18–27 nm, 4 m ² /g
MnO _x -NG-1.0	Glycine, $\varphi = 1.00$	Mn ₃ O ₄ + [MnO]	19–22 nm, 40 m ² /g
MnO _x -NG-1.25	Glycine, $\varphi = 1.25$	Mn ₃ O ₄ + [MnO]	19–20 nm, 18 m ² /g
MnO _x -NG-1.5	Glycine, $\varphi = 1.50$	Mn ₃ O ₄ + [MnO]	20–22 nm, 14 m ² /g
MnO _x -NC-1.0	(NH ₄) ₃ Cit	Mn ₂ O ₃	20–22 nm, 14 m ² /g
MnO _x -NCG-1.0	(NH ₄) ₃ Cit + Glycine	Mn ₃ O ₄	11.3 nm, 24 m ² /g
MnO _x -NCU-1.0	(NH ₄) ₃ Cit + Urea	Mn ₃ O ₄	9.3 nm, 35 m ² /g

¹ In square brackets a minor product is depicted. ² Estimated from XRD data with Scherrer equation.

Manganese nitrate tetrahydrate ($\text{Mn}(\text{NO}_3)_2 \cdot 4\text{H}_2\text{O}$) from Fischer Scientific (Illkirch, France), CAS: 20694-39-7, $\geq 97.5\%$ purity, analytical, is used as the precursor source of manganese and nitrate. The fuels are from Thermo Scientific Chemicals (Illkirch, France), glycine (CAS: 56-40-6, 99% purity) and urea (CAS: 57-13-6, 99% purity, ACS reagent). The additional ligand is anhydrous ammonium citrate tribasic ((NH₄)₃Cit) (Sigma Aldrich, Saint Louis, MO, USA, $\geq 97\%$ purity, CAS: 3458-72-8). Depending on the mixture, the reactants are added in a 250 mL Erlenmeyer flask with 10 mL of ultrapure water (18.2 MOhm·cm, TOC < 1 ppb) produced by the UltraAnalytique Veolia device (Veolia Water STI, Decines, France). The mixture is agitated for approximately 10 min until dissolution of all remaining crystals, followed by a 20 min sonication bath treatment. The Erlenmeyer flask is then

placed in an oven at 80 °C for 48 h for slow evaporation of the water solvent to obtain a dried xerogel. For the synthesis, the Erlenmeyer flask is placed on an already heated plate at 350 °C to undergo auto-ignition. The self-propagating combustion is usually performed in 30–60 s, accompanied by gas evaporation. After letting the flasks cool down, ultrapure water is added and another step of the sonication bath is performed for 5 min to disperse all the obtained particles. The dispersion is then filtered and washed using water. Finally, the powder is dried overnight at 80 °C prior to characterization. The obtained powder generally yields at 90% according a theoretical 1.0 g of desired phase product (i.e., Mn₃O₄).

2.2. Physicochemical Characterization of Manganese Oxides

Scanning electronic microscopy (SEM) imaging was performed using a Zeiss (Oberkochen, Germany) 2600F microscope with a resolution of 5 nm. The carbon samples were deposited on a conductive carbon tape. X-ray diffraction (XRD) measurements were performed using a Bruker (Karlsruhe, Germany) D-8 Advance diffractometer with a Cu K α source ($\lambda = 1.54184 \text{ \AA}$). The analysis of the XRD diagram was performed using EVA Bruker software (version 09.2017) with a COD database. The reference cards for the detected phases are COD 1514106 (cubic) for byxbite (Mn₂O₃); COD 1514121 (tetragonal) for hausmannite (Mn₃O₄); and COD 1010436 (cubic) for manganosite (MnO). The size of the crystallites is calculated using the Scherrer equation:

$$d_{XRD} = \frac{K\lambda}{\beta \cos \theta}$$

where K is a shape factor ($K = 1$ is taken) and β is a FWHM of the reflex detected at θ angle. The strongest reflex for the given crystalline phase was always taken for the analysis.

ATR-FTIR measurements were performed using a ThermoFisher (Illkirch, France) IR spectrometer equipped with ATR Smart Orbit setup. Gas adsorption–desorption measurements were performed using an ASAP 2420 Micromeritics analyzer measuring the N₂ physisorption isotherm at 77 K after degassing the samples at 150 °C for 12 h. Thermogravimetric analysis (TGA) was performed with a Q 5000 TA Instrument under air using platinum crucibles from room temperature to 800–900 °C with 5 °C/min ramp.

Temperature-Dependent Diffuse Reflectance Infrared Fourier Transform Spectroscopy (TD-DRIFTS) was performed using a Vertex 70 Bruker IR spectrometer (4000 cm⁻¹ to 600 cm⁻¹) equipped with a one-pot sample compartment. The setup is equipped with a homemade chamber (ca. 7 mL of volume) for temperature-controlled analyses with ZnSe windows and a Praying Mantis™ diffuse reflectance accessory from Harrick. The samples were diluted with KBr prior to analysis in the holder and purged with helium first. Then, the tests were conducted with air flow (5 mL/min) with heating ramp of 2 °C/min, up to a maximum 440 °C.

2.3. Electrochemical Measurements

2.3.1. Ink Preparation

First, a certain amount of oxide powder (active material), Vulcan XC-72 (conductive agent), and Nafion 0.5 wt.% (binder) are taken and all the products are weighted to obtain a 70:25:5 ratio, respectively. The active material and conductive agent are mixed together in an agate mortar. Inks are prepared by adding a desired amount of the prepared mixture in a glass vial and the required volume of ultrapure water and Nafion 0.5 wt.% are added to obtain a 2 g/L concentrated ink. The ink is then shaken and sonicated in an ultrasonication bath for 20 min.

2.3.2. Ink Deposition on Glassy Carbon Rod

The active material is deposited by drop casting onto the surface of a glassy carbon rod electrode of 6 mm radius. The total deposited volume of ink is 75 μL divided by 5 deposition steps of 15 μL in which the electrode is dried for 10 min in an oven at 80 $^{\circ}\text{C}$ between each step. The loading of active material is approximated to 0.75 mg/cm^2 . A final deposition of 15 μL Nafion 0.5 wt.% in a mixture of lower aliphatic alcohols and water is added and dried to act as a binder.

2.3.3. Three-Electrode Cell Set-Up

A three-electrode cell inside a Faraday cage is used for the electrochemical tests. First, 100 mL 1 M NaOH electrolyte is poured in the cell, followed by the addition of a platinum wire with a coil end counter electrode in the compartment separated by a fritted and a mercury/mercurous oxide electrode (Hg/HgO) in 1 M NaOH internal solution in the compartment separated by a Luggin capillary. The solution in the cell is then purged for at least 30 min under N_2 gas. The glassy carbon rod electrode with active material—the working electrode—is placed in a holder and then placed inside the electrochemical cell in order to only have contact with the surface of the electrode. The N_2 gas is flushed above the electrolyte to keep a controlled atmosphere without O_2 . The electrodes are connected to a SP-300 potentiostat from BioLogic (Grenoble, France).

3. Results

3.1. Mechanism of Conventional Nitrate–Glycine Synthesis

3.1.1. FTIR and TGA Analysis of Decomposition Processes

Figure 1A shows ATR-FTIR spectra of selected solid products at ambient temperature: the Mn(II) nitrate, glycine, and their mixtures with different molar ratio φ . The solids were prepared by complete evaporation of water from their aqueous solutions at 80 $^{\circ}\text{C}$ for 48 h. The attribution of the main IR bands is given in Table 2. In general, the spectra are in agreement with the structure of hydrated $\text{Mn}(\text{NO}_3)_2$ [20] and zwitterion solid glycine [21,22], as reported in the literature. Noticeably, the FTIR spectrum of $\text{Mn}(\text{NO}_3)_2 \cdot 4\text{H}_2\text{O}$ shows a complex ν_{OH} band in the 3200–3600 cm^{-1} region, containing several contributions. In the symmetrical octahedral structure of the $\text{Mn}(\text{NO}_3)_2 \cdot 4\text{H}_2\text{O}$ complex, the position of all water molecules is equivalent [23]. Thus, the complex nature of the ν_{OH} band is due to a different coordination energy of water ligands forming H-bonds between themselves and with nitrate ligands. In particular, a sharp ν_{OH} band at $\approx 3350 \text{ cm}^{-1}$ can be attributed to H_2O ligands weakly coordinated by intermolecular hydrogen bonds, while a broader band located at lower wavenumbers is associated with water ligands forming a long-range order intermolecular H-bonded network.

The IR spectrum of dried nitrate–glycine mixtures contains the similar IR bands of nitrate ligand (ν_1 – ν_6) as Mn nitrate nearly at the same positions. The ν_{OH} band is gradually distorted as the ratio of glycine-to-nitrate φ increases: for $\varphi = 2$, a relatively broad band centered at $\approx 3500 \text{ cm}^{-1}$ is observed, indicating disruption of the network of H-bonded water ligands. On the other hand, the IR bands of glycine are modified and shifted in the presence of Mn(II) nitrate comparing with pure glycine. Most remarkable is the absence of the peaks of $\delta_s(\text{NH}_3^+)$ at 1510 cm^{-1} and $\rho(\text{COO}^-)$ at 610 cm^{-1} , and wider separation of peak $\nu_a(\text{COO}^-)$, which shifts from 1604 cm^{-1} to 1633 cm^{-1} , and peak $\nu_s(\text{COO}^-)$, which shifts from 1412 cm^{-1} to 1390 cm^{-1} . We attribute these changes to the formation of a Mn–Gly complex [24,25] after the drying step, which also has been previously suggested [26] as part of a mechanism of Mn nitrate–glycine SCS. Considering the presence of non-modified IR peaks related to NO_3^- in the spectrum of the mixture, and stoichiometry between nitrate and glycine, one may tentatively suggest the formation of a $[\text{Mn}(\text{gly})(\text{H}_2\text{O})_4](\text{NO}_3)_2$ or

[Mn(gly)(H₂O)₂](NO₃)₂ complex after the drying step. It is not possible to evaluate more exactly the composition of the dried solids based on only ATR-FTIR data.

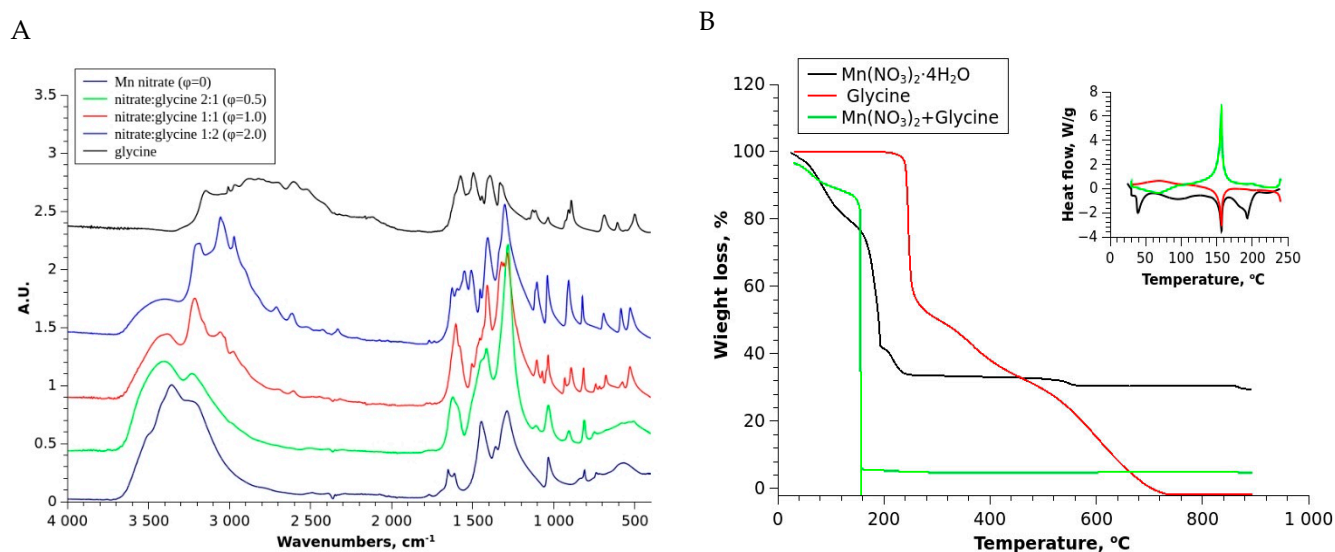


Figure 1. ATR-FTIR spectra of dried precursors Mn(NO₃)₃·4H₂O and glycine, and their mixture with different ratios (A); TGA curves of in-air decomposition of Mn(II)nitrate, Glycine, and their dried mixture (B); inset is the heat flow resulting from decomposition reaction.

Table 2. IR peak attributions for the manganese nitrate–glycine mixture.

Precursor	IR Band (Position cm ⁻¹ , Observation) ¹	Attribution
Mn(NO ₃) ₂ ·4H ₂ O	3430, st.br.	ν(OH)
	3185, s.	
	2736, m.	
	2147, m.	
	1762, st., s.	ν ₁ + ν ₄
	1601, st., s.	2 ν ₂
	1435, sh.	ν ₃ (NO ₃ ⁻)
	1367, st.	ν ₃ (NO ₃ ⁻)
	1055, st.	ν ₁ (NO ₃ ⁻)
826, st.	ν ₂ (NO ₃ ⁻)	
Glycine, NH ₂ CH ₂ COOH	3165, w, sh.	ν _a (NH ₃ ⁺)
	2820, w	ν _s (CH)
	2610,	ν _s (NH ₃ ⁺)
	2120, m	ν _a (COO ⁻) + τ (NH ₃ ⁺)
	1604	ν _a (COO ⁻)
	1510	δ _s (NH ₃ ⁺)
	1412	ν _s (COO ⁻)
	1330	δ (CH ₂) + δ (NH ₂)
	1110	ρ (NH ₃ ⁺)
	1030	tw. (NH ₂)
	890	δ (NH ₂) + δ (CH ₂)
	690	ρ (COO ⁻)
610	ω (COO ⁻)	

¹ st. = strong, m. = medium, w = weak, br. = broad, s. = sharp, sh. = shoulder.

TGA curves in the air decomposition of a Mn nitrate–glycine mixture also differs from the curves of pure solids (Figure 1B). Most remarkable is the sharp drop of the mass of a nitrate–glycine mixture at ca. 170 °C, contrasted to the fast gradual mass decrease of separated nitrate and glycine, occurring at somewhat higher temperatures. This sharp decrease points to the instantaneous character of the decomposition reaction of the nitrate–glycine mixture. Moreover, this decomposition results in the formation of a large number of gas

products; due to the fast escape of these products, the measured mass of the remaining solids is strongly underestimated, or even drops to zero at one point. Once the decomposition is finished, the further mass measurements are expected to be correct. However, one should note that the weight remaining after this sharp drop (5%) is smaller than what is expected for $\text{Mn}(\text{NO}_3)_2$ decomposition into Mn_3O_4 (30.4%), indicating that a significant part of the solid product is blown away by the evolving gasses.

In order to have a more detailed interpretation of the processes happening during these decomposition reactions, we performed temperature-dependent DRIFT analysis of the composition of Mn(II) nitrate, glycine, and their dried mixture (Figure 2). The interpretation of DRIFT spectra and TGA curves for each of the studied solid precursors is given below.

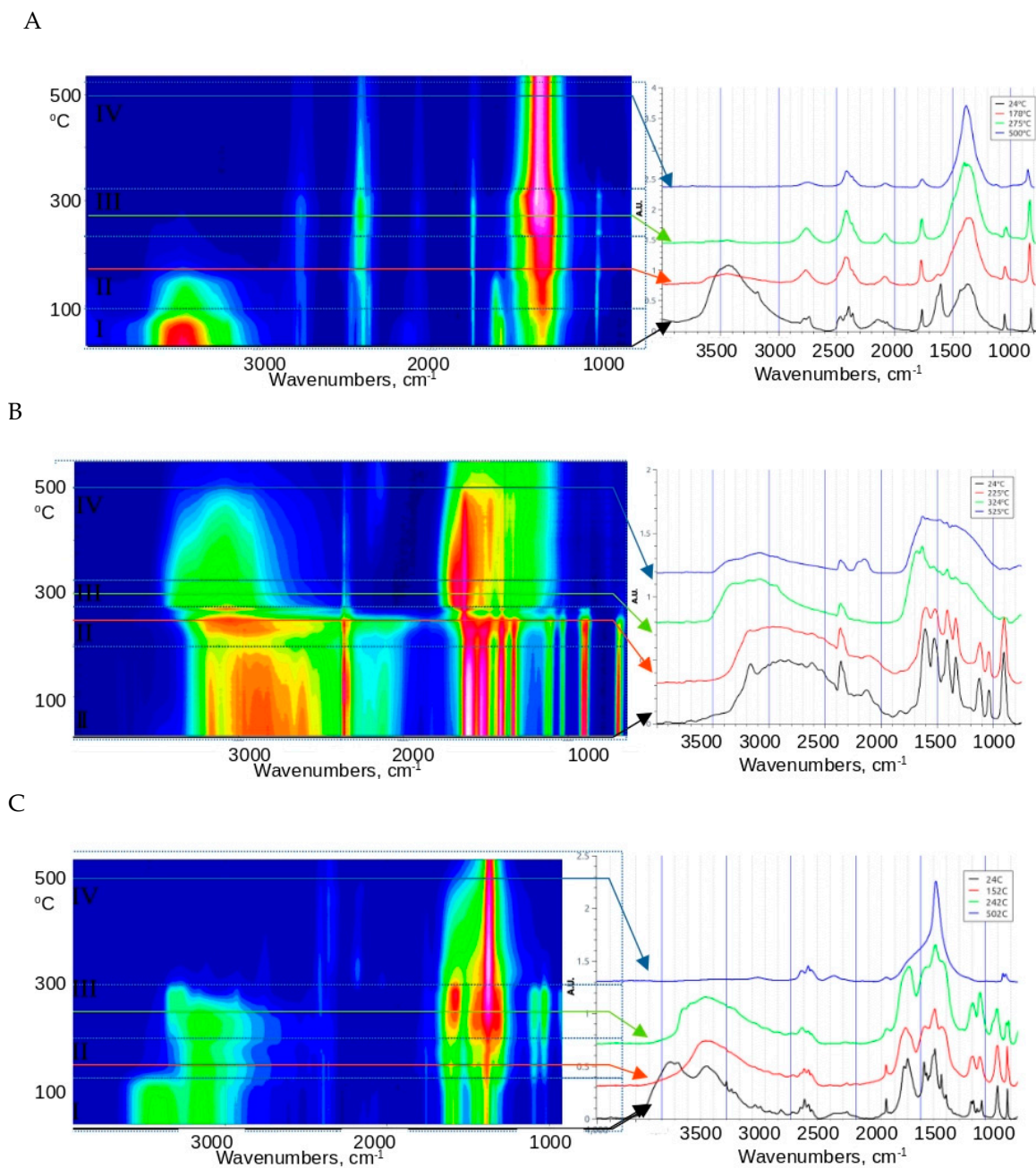


Figure 2. DRIFT spectra of $\text{Mn}(\text{NO}_3)_2$ (A), glycine (B), and their dried 1-1 mixture (C); the arrows shows the temperature for which the slice spectra are shown at the right side.

3.1.2. Mn(II) Nitrate

As the TGA curve shows, in the range from ambient temperature to ca. 100–120 °C, there is gradual dehydration of $\text{Mn}(\text{NO}_3)_2 \cdot 4\text{H}_2\text{O}$; the weight loss at 120 °C corresponds to the loss of two molecules of H_2O per nitrate, i.e., formation of $\text{Mn}(\text{NO}_3)_2 \cdot 2\text{H}_2\text{O}$. The IR peaks of nitrate remaining nearly unchanged in this temperature range, while peaks of $\nu(\text{OH})$ at 3400 cm^{-1} and $\delta(\text{HOH})$ at 1650 cm^{-1} are gradually disappearing. In the range 120–180 °C, the weight loss is accelerating, reaching $\text{Mn}(\text{NO}_3)_2 \cdot \text{H}_2\text{O}$ stoichiometry at 140–150 °C. At ca. 180 °C, the weight loss corresponds to anhydrous $\text{Mn}(\text{NO}_3)_2$; however, it is not possible to exactly evaluate the stoichiometry of the remaining solid above 150 °C because of the onset of low-temperature $\text{Mn}(\text{NO}_3)_2$ decomposition assisted by water evaporation [19]. In fact, anhydrous $\text{Mn}(\text{NO}_3)_2$ decomposes only at temperatures above 200 °C [19,27], while decomposition of hydrated complex starts at ≈ 150 °C.

The IR peaks related to nitrate (see Figure 2A) are changing in the range 120–180 °C: the intensities of peaks ν_1 – ν_4 in the range 1300 – 1600 cm^{-1} are decreasing, and the peaks are gradually transforming into a strong single IR peak centered around 1380 cm^{-1} . The latter peak remains relatively strong up to a high temperature (above 500 °C). Similar changes in nitrate IR bands have been observed for alkaline metal nitrates above melting point [28], and explained by the fusion of nitrate salt. The nitrate IR bands remaining even at high temperature have been observed before [29] and attributed to the remaining traces of nitrate, most probably in a molten state. We note also that this strong band at 1500 cm^{-1} is absent in the ATR-FTIR spectra of the final product after filtering, washing, and drying.

The weight of nitrate sample is stabilized at ca. 220 °C at the value of 35% of the initial mass, corresponding to the formation of MnO_2 . At $t > 550$ °C, there is an additional 5% of weight loss indicating transformation of MnO_2 to Mn_2O_3 . Reported results are in agreement with reported studies of $\text{Mn}(\text{NO}_3)_2$ thermal decomposition [20,27,29]. The weight loss measured at the transformation of dehydrated $\text{Mn}(\text{NO}_3)_2$ to MnO_2 suggest formation of an unstable intermediate of oxonitrate $\text{MnO}_x(\text{NO}_3)_{2-x}$ at ca. 180 °C [20,29]. However, no direct experimental evidence of formation of this intermediate has ever been reported. The presented DRIFT spectra also do not allow us to claim or to reject the observation of an oxonitrate intermediate.

It is important to note that the main gaseous products of hydrated $\text{Mn}(\text{NO}_3)_2$ decomposition at 180 °C are NO_2 and NO , and N_2O in a smaller quantities [29], while O_2 is produced in significantly smaller amounts compared with nitrogen oxides. A noticeable amount of oxygen is formed around 500 °C and again above 600 °C due to transformation of MnO_2 first to Mn_2O_3 and then to Mn_3O_4 . Nevertheless, the total amount of oxygen produced by Mn nitrate decomposition is smaller than stoichiometric. This is an important observation, considering that the calculation of fuel-to-salt ratio φ is typically based on the assumption stoichiometric quantity of oxygen produced by the decomposition of nitrate. Considering this uncertainty in the stoichiometry of O_2 production from nitrates decomposition, it makes more sense to calculate the value of fuel-to-salt ratio φ simply as a molar ratio of nitrate and fuel precursors, rather than base it on the stoichiometry of reactions (1)–(3).

For the comparison with the decomposition of the nitrate–glycine mixture, it is important to note now that, according to the thermodynamic analysis of thermal decomposition of hydrated $\text{Mn}(\text{NO}_3)_2$, dehydration of Mn nitrate requires relatively low activation energy (ca. 60 kJ/mol), while its decomposition has a much higher activation barrier (210 kJ/mol).

3.1.3. Glycine

There are no changes in the structure of glycine below ca. 220 °C, as indicated by no weight losses in TGA and no changes in DRIFT spectra. However, in the range 220–230 °C

there is a significant weight loss of ca. 50%. In DRIFT spectra (Figure 2B), one observes a new pair of peaks at 1640 cm^{-1} and 1680 cm^{-1} , and a broad peak at $3300\text{--}3500\text{ cm}^{-1}$, which can be attributed to $\nu(\text{C}=\text{O})$ of primary and secondary amides, and $\nu(\text{N-H})$ of amides. The analysis of gaseous products of glycine decomposition at a temperature of $220\text{--}230\text{ }^{\circ}\text{C}$ demonstrated the formation of NH_3 [21] as well as H_2O and CO_2 , while liquid phase products included various amides (formamide, acetamide, N-butylacetamide, n-butyramide, and propionamide) and diones [22]. We propose that, at $t > 220\text{ }^{\circ}\text{C}$, the zwitterion structure of glycine is disrupted, and glycine is losing some of amino groups, producing gaseous ammonia, while the remaining amino groups are involved in the formation of oligomeric amide-type intermediates [22].

At temperatures above $230\text{ }^{\circ}\text{C}$, one observes continuous weight loss, which is completed at ca. $620\text{ }^{\circ}\text{C}$, when no solid residues are remaining. In DRIFT spectra, in this temperature range one observes a gradual decrease in all observed IR peaks. The strongest remaining peaks are detected in the range of $3000\text{--}3150\text{ cm}^{-1}$ (broad peak) and 1640 cm^{-1} . The appearance of these peaks is similar to the IR spectra of formamide and acetamide, and can be attributed to $\nu(\text{N-H})$ and $\nu(\text{C}=\text{O})$ in amides, thus confirming the formation of various amides as products of glycine decomposition [21]. The amides and diones are the main products of glycine endothermic decomposition in an oxygen-lean atmosphere [21,22].

It is noteworthy that the TGA behavior of dried glycine below $230\text{ }^{\circ}\text{C}$ is the same in air, as observed in the present work, and under N_2 [30]. The main difference occurs at higher temperatures: under N_2 the remaining weight is above 20%, even at $900\text{ }^{\circ}\text{C}$, while it drops to 0% above $600\text{ }^{\circ}\text{C}$ in air. Thus, the presented TGA and DRIFT data suggest that the thermal decomposition of glycine in air also proceeds via first endothermic formation of amide-type intermediates, similarly to an oxygen-lean atmosphere. However, in air these intermediates are eventually oxidized at temperatures above $230\text{ }^{\circ}\text{C}$, and totally decomposed above $600\text{ }^{\circ}\text{C}$.

Kinetic studies of glycine decomposition gave evidence that the first step (glycine-to-amides transformation) is a topochemical reaction, requiring formation of reaction nucleation sites, and a certain incubation period, the length of which depends on the temperature [21]. After the induction period, the rapid growth of the decomposition rate is observed, which may explain the relatively sharp weight loss detected by TGA at $220\text{ }^{\circ}\text{C}$. Then the rate of decomposition is reaching the constant plateau, limited by the rate of reaction propagation. The second step of decomposition above $230\text{ }^{\circ}\text{C}$ follows the kinetics of solid state thermal decomposition [30], and is characterized by relatively high activation energy ($150\text{--}159\text{ kJ/mol}$) [21,30].

3.1.4. Nitrate–Glycine Dried Solid Mixture ($\varphi = 1$)

Thermodynamic [31] and polarographic [32] studies suggest that glycine forms relatively weak complexes with Mn^{2+} , compared with other cations, such as Cu^{2+} , and Zn^{2+} . Above the temperature of dehydration, the Mn-Gly complexes are decomposing into products similar to pure glycine. However, the temperature of dehydration of complexes may be somewhat higher than that of pure glycine [18].

In the temperature range from ambient to $170\text{ }^{\circ}\text{C}$, one observes slow weight loss of the glycine-nitrate mixture, simultaneous with a strong decrease in the intensity of the $\nu(\text{OH})$ broad peak at $3450\text{--}3600\text{ cm}^{-1}$ (see Figure 2C). One may suggest that dehydration of the mixture occurs in this temperature range, similar to one observed in the case of pure $\text{Mn}(\text{NO}_3)_2 \cdot 4\text{H}_2\text{O}$. The weight loss at $170\text{ }^{\circ}\text{C}$ is ca. 6%, corresponding to the loss of one H_2O entity of $[\text{Mn}(\text{gly})(\text{H}_2\text{O})_4](\text{NO}_3)_2$ (5.5%) or $[\text{Mn}(\text{gly})(\text{H}_2\text{O})_2](\text{NO}_3)_2$ (6.2%): the accuracy of our TGA measurements does not allow us to distinguish between two possible compositions of a dried solid mixture of nitrate–glycine.

At 170 °C, very sharp weight loss is detected. This temperature is below the onset of decomposition of pure glycine (220 °C), suggesting the decomposition of the glycine complex of Mn formed upon the drying step. The weight loss during the decomposition of this complex is remarkably sharper than in the case of decomposition of pure nitrate or glycine, and points to the autocatalytic character of the decomposition. Contrary to the endothermic decomposition steps of pure Mn(II) nitrate and glycine, the decomposition of the Mn glycine complex is exothermic (inset of Figure 1B), which may explain the autocatalytic kinetics of the reaction. Alternatively, the products of the initial decomposition of the complex, in particular ammonia and water vapor, may act as a catalyst of further decomposition of the Mn glycine complex. In TGA curves, the weight drop to ca. 5% of mass, which remains stable up to 600 °C, can be attributed to solid Mn oxide. The remaining mass is significantly lower than one expects for MnO₂ (29.6%) or Mn₃O₄ (26.0%), undoubtedly indicating the loss of solid products due to the eruptive evolution of the gas products of decomposition.

Interestingly, the DRIFT spectra do not demonstrate the same sharp changes in bands appearance. It may be related to the fact the DRIFT analysis is performed with the solids mixed with KBr as a mean to adjust the intensity of IR signals. Dilution of the solid mixture by a neutral component changes the conditions of reaction self-propagation. Another interesting point is that, contrary to decomposition of pure glycine, no clear indication of formation of amide-related IR peaks ($\nu(\text{N-H})$ at 3300–3500 cm⁻¹ and $\nu(\text{C=O})$ at 1640–1680 cm⁻¹) during the decomposition of its complex with Mn(II) have been observed, indicating a different mechanism of decomposition of pure glycine and glycine as a ligand in the complex with Mn(II).

3.2. Analysis of the Products of SCS with Nitrate–Glycine Mixture

XRD diagrams of manganese oxides synthesized by the nitrate–glycine SCS method are depicted in Figure 3 for a varied fuel-to-salt ϕ ratio. In the case of the nitrate–glycine mixture, for all ϕ values, a mixture of oxides are obtained. All oxides demonstrate a typical mesoporous structure of partially agglomerated oxide nanoparticles with the size in the range 25–40 nm (Figure 3B).

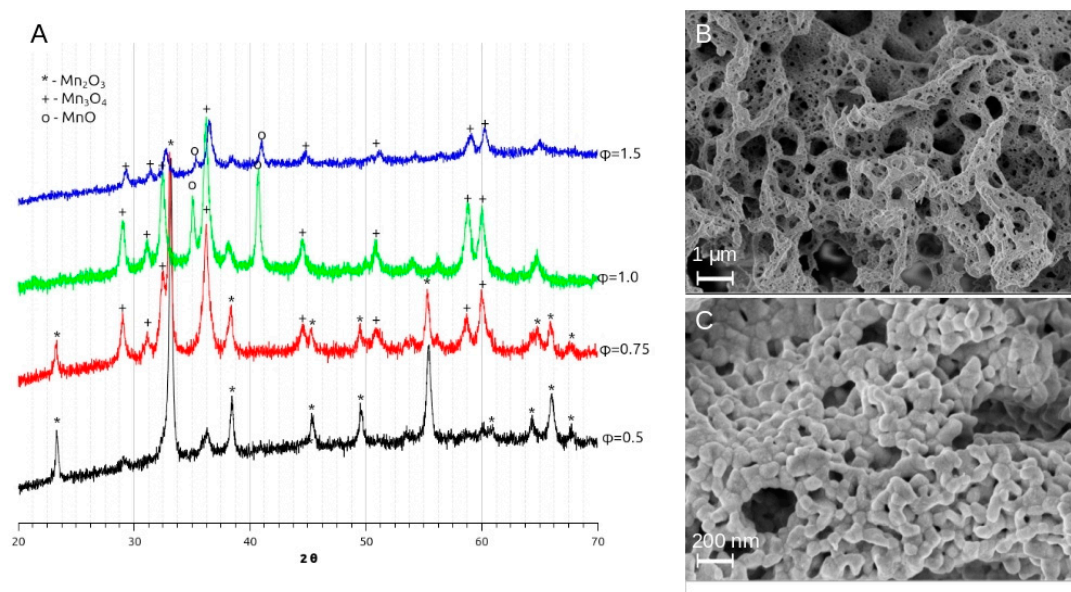


Figure 3. XRD diagrams of Mn oxides MnOx-NG, prepared by SCS with nitrate–glycine mixture with different fuel-to-salt ratio ϕ (A). Typical SEM images of Mn oxide prepared by SCS with 1:1 nitrate–glycine mixture (B,C).

At low $\varphi < 1$, Mn_2O_3 is the main phase, while, for $\varphi \geq 1$, the $\text{Mn}_3\text{O}_4 + \text{MnO}$ mixture is formed. The same trend of formation of a more reduced oxide for higher φ had been observed before [26,33]. According to the Mn-O phase diagram [34], the formation of more reduced oxides is thermodynamically preferable under the conditions of (i) higher temperatures and (ii) lower partial O_2 pressure, p_{O_2} . In particular, at $p_{\text{O}_2} = 1$ bar, the temperature ranges of thermodynamic stability of Mn oxides are as following:

- MnO_2 : ambient to $t \text{ } ^\circ\text{C} < 461 \text{ } ^\circ\text{C}$;
- Mn_2O_3 : $461 \text{ } ^\circ\text{C} < t \text{ } ^\circ\text{C} < 755 \text{ } ^\circ\text{C}$;
- Mn_3O_4 : $755 \text{ } ^\circ\text{C} < t \text{ } ^\circ\text{C} < 1292 \text{ } ^\circ\text{C}$;
- MnO : above $1292 \text{ } ^\circ\text{C}$.

This temperature ranges are in full agreement with our TGA results (Figure 1B) and study of slow thermal decomposition of $\text{Mn}(\text{NO}_3)_2 \cdot 4\text{H}_2\text{O}$ in air: the main product of the decomposition up to ca. $485\text{--}500 \text{ } ^\circ\text{C}$ is MnO_2 , while at temperatures above $520 \text{ } ^\circ\text{C}$ oxide Mn_2O_3 is the main product [27].

As the decomposition of a fuel is a main source of heat generation during SCS, an increase in φ is expected to result in a higher reaction temperature. Thermodynamic models of SCS predicts that the adiabatic temperature, T_{ad} [31] is attained if stoichiometric quantities of nitrate/glycine are used, i.e., $\varphi = 0.89$. A further increase in φ is expected to result in a slight decrease in SCS temperature due to stronger heat loss by escape of hot gaseous products, formed in quantities from fuel bigger than from nitrate decomposition. However, experimentally an increase in the reaction temperature up to $\varphi \approx 1$ or even further is typically observed, while no decrease in synthesis temperature with an increase in φ is detected. Thus, the formation of Mn_2O_3 for low φ and $\text{Mn}_3\text{O}_4 + \text{MnO}$ for $\varphi \geq 1$ can be explained by an increase in SCS temperature with a higher content of glycine. It also may explain the decrease in BET surface area of oxide with an increase in glycine content, which results in stronger sintering of oxide nanoparticles due to the higher temperature of the SCS reaction. In fact, the highest surface area of $40 \text{ m}^2/\text{g}$ is obtained with MnOx-NG-1 oxide, resulting from the optimal conditions for heat generation.

3.3. SCS Synthesis with Ammonium Citrate: Nitrate–Citrate, Nitrate–Citrate–Glycine, and Nitrate–Citrate–Urea

3.3.1. Thermal Stability Studies with Nitrate–Citrate, Nitrate–Citrate–Glycine, and Nitrate–Citrate–Urea SCS Mixtures

In order to better understand the role of the formation of intermediate compounds and complexes during the drying step of SCS, we performed the similar study of SCS processes with a Mn(II)–nitrate mixture with ammonia citrate as a complexing agent and a sole fuel, as well as in combination with glycine and urea as fuels. The study was performed with 1-1-1 molar ratio mixtures of Mn nitrate, ammonia citrate, and an additional fuel.

Citrate is strong chelating anion and readily forms stable complexes with Mn(II) [35–38], thus preventing formation of hydroxide. Tri-basic ammonium citrate was chosen as the source of citrate ions due the fact that the pH of its solution is close to 7, similar to glycine and urea solutions, ensuring comparable conditions of drying step. Also, the exchange of anions with Mn(II) in solution results in the formation of ammonium nitrate [39–41], which upon drying and heating decomposes with a strong exothermic effect, thus favoring SCS conditions.

The pH of an aqueous solution of $(\text{NH}_4)_3\text{Cit}$ is close to 7, while the solution of $\text{Mn}(\text{NO}_3)_2$ and $(\text{NH}_4)_3\text{Cit}$ has $\text{pH} = 4.6$. At this pH, citrate is reported to form strong and stable complexes with Mn(II) salts [42]. The structure of complexes formed at a slightly acidic pH is disputed: both monodentate complex $(\text{NH}_4)_4[\text{Mn}(\text{Cit})_2]$ [35] and binuclear bidentate $(\text{NH}_4)_{2n}[\text{Mn}_2(\text{HCit})_2(\text{H}_2\text{O})_2]_n$ [36] are suggested as based on XRD

and FTIR characterization. At higher pH = 7.0–8.0, the mononuclear complex of Mn(III), namely $(\text{NH}_4)_5[\text{Mn}(\text{Cit})_2] \cdot 2\text{H}_2\text{O}$, is formed due to a simultaneous reaction with dissolved oxygen [35].

Figure 4A shows the FTIR spectra of dried $\text{Mn}(\text{NO}_3)_2$, $(\text{NH}_4)_3\text{Cit}$, and their mixtures with glycine and urea. The FTIR spectra of $(\text{NH}_4)_3\text{Cit}$ are in agreement with the literature, namely characteristic broad IR band of carbonyl $\nu(\text{O-H})$ at ca. 3200 cm^{-1} , broad $\nu(\text{N-H})$ at 2700 cm^{-1} , a pair of bands of $\nu_s(\text{COO}^-)$ at 1400 cm^{-1} and $\nu_a(\text{COO}^-)$ at 1575 cm^{-1} , and $\nu(\text{C-OH})$ at 1260 cm^{-1} . In the case of a Mn nitrate–citrate dried mixture, one observes an additional strong and broad $\nu(\text{O-H})$ band related to water ligand presence. One may also notice a stronger separation between the centers of bands of $\nu_s(\text{COO}^-)$ at 1390 cm^{-1} and $\nu_a(\text{COO}^-)$ at 1610 cm^{-1} , which can be explained by a stronger coordination of citrate to manganese. On the other hand, these bands have clearly more contributions compared with pure $(\text{NH}_4)_3\text{Cit}$, which may be an indication of various forms of coordination of citrate with Mn, for example co-existence of both mono- and bidentate citrate in the dried mixture. This non-uniformity can be anticipated, considering that the structure of the complex depends on both the metal–ligand ratio and pH of solutions, which can be changing during the evaporation of solvent. The appearance of a small sharp band at 1750 cm^{-1} in the case of the Mn(II) nitrate and citrate mixture can be attributed to $\nu(\text{C=O})$ stretching vibration, related to partial protonation of citrate and formation in slightly acidic solution of Mn nitrate: for citric acid $pK_{a1} = 3.18$, $pK_{a2} = 4.761$, and $pK_{a3} = 6.396$, and thus H_2Cit^- is expected to be a predominant citrate anion at pH = 4.5.

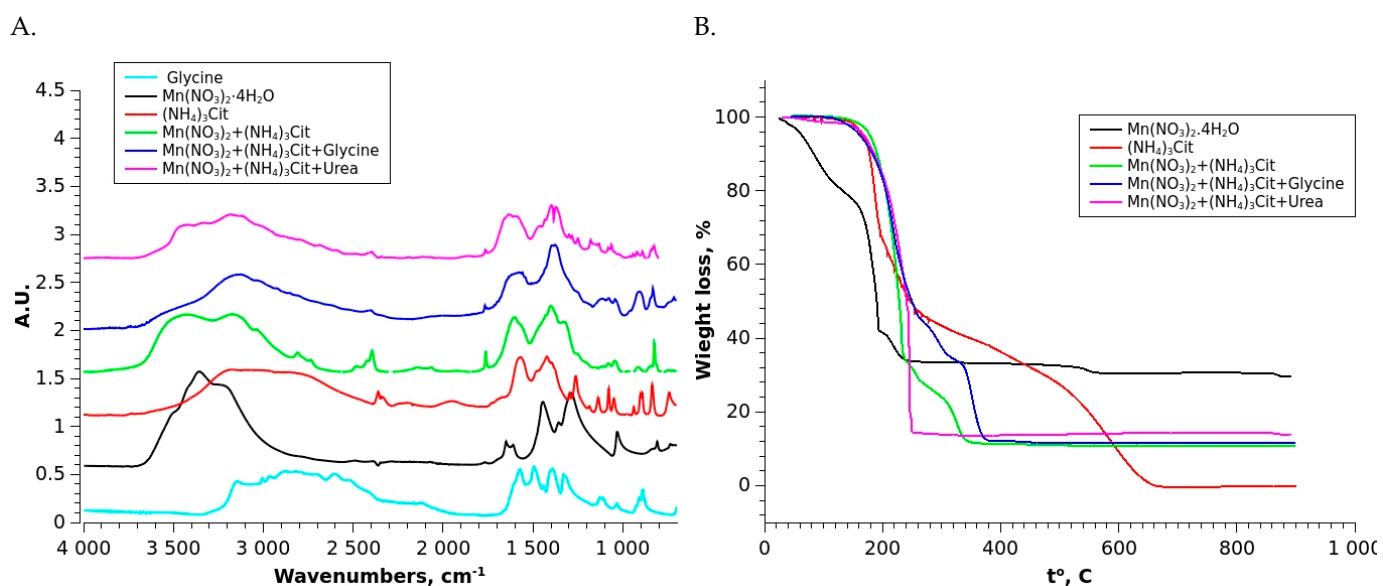


Figure 4. ATR-FTIR spectra of SCS solid mixtures with ammonium citrate (A); TGA curves of in-air decomposition of SCS solid mixtures (B).

In the case of dried solutions of Mn nitrate and ammonium citrate with glycine or urea, a much lower intensity of the $\nu(\text{OH})$ stretching band at 3600 cm^{-1} is observed, which may be an indication that water ligands are substituted by glycine or urea in this case. The band of $\nu_a(\text{COO}^-)$ at $1580\text{--}1620\text{ cm}^{-1}$ is superposed with $\nu(\text{C-N})$ expected at $1590\text{--}1605\text{ cm}^{-1}$, which makes the analysis of their expected positions complicated. However, FTIR spectra are in agreement with assumption of formation of a strong Mn(II) complex with citrate ligands also in the presence of glycine or urea in the initial solution.

TGA curves of the decomposition of the ammonium citrate and its mixture with Mn nitrate and with Mn nitrate and glycine are shown in Figure 4B. The thermal decomposition of ammonium citrate has not yet been studied in detail. The crystal structure of

solid ammonium citrates is determined by hydrogen bonds, predominantly by N-H...O bonds [43], which are relatively weak and break with temperature. Thus, one may expect that thermal decomposition of ammonium citrate would have a similar mechanism to citric acid decomposition, which is a two-step process [44,45]. Namely, the first step occurs simultaneously with melting of citric acid above 150 °C and results in the formation of a few stable intermediates, mostly *cis*- and *trans*-aconitic acid [45]. The intermediates are then slowly dehydrated, forming corresponding anhydrides until total decomposition above 600 °C.

The dried mixture of Mn nitrate and ammonium citrate is stable up to the temperature of ≈ 150 °C before the decomposition of citrate starts. DRIFT spectra (Figure 5A) show only the loss of water, as indicated by the disappearance of the $\nu(\text{OH})$ band at 3600 cm^{-1} in this temperature range. At temperatures above 200 °C, the TGA curve shows a rapid mass loss, in agreement with the fast and simultaneous decrease in intensity of IR bands attributed to nitrate and citrate detected above 150 °C in DRIFT spectra. The decrease in the intensities of carbonyl-related bands ($\nu(\text{OH})$ at 3200 cm^{-1} and $\nu(\text{C-OH})$ at 1215 cm^{-1}) occurs at lower temperatures (150–200 °C) compared with the carboxylate ($\nu_s(\text{COO}^-)$ at 1390 cm^{-1} and $\nu_a(\text{COO}^-)$ at 1610 cm^{-1}) groups, which starts above 200 °C. It confirms that the mechanism of decomposition of the Mn–citrate complex is similar to the one of the decomposition of citric acid and proceeds first via elimination of the carbonyl group of citrate and formation of aconate-type intermediates [45]. Contrary to the slow second step of the decomposition of pure ammonium citrate, the decomposition of the nitrate and citrate mixture is nearly finished above 340 °C, according to TGA. At the same temperature, in DRIFT spectra one observes only remaining IR bands attributed to the rest of the nitrate, as in the case of pure Mn nitrate decomposition, or Mn nitrate–glycine SCS synthesis, described in the previous section. One may suggest that Mn acts as a catalyst of the decomposition of citrate ligands, resulting in its faster decomposition compared with pure ammonium citrate. A strong band centered at 602 cm^{-1} appears above 300 °C, and can be attributed to $\nu(\text{Mn-O})$ stretching, reported for MnO_2 and Mn_2O_3 oxides [46].

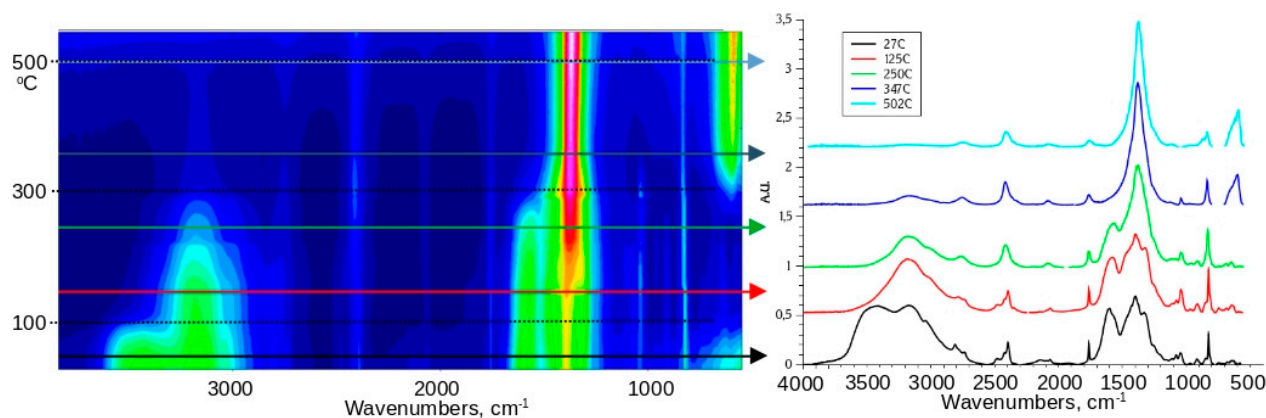
The thermal decomposition of the Mn nitrate–ammonium citrate–glycine mixture is similar to that of the nitrate–citrate mixture, indicating that the presence of glycine does not influence the decomposition mechanism of the manganese citrate complex. Contrary to the nitrate–glycine mixture, there is no indication of autocatalytic decomposition of dried precursors either in the case of nitrate–citrate or in the case of nitrate–citrate–glycine mixtures. The stable weight remaining after the decomposition above 200 °C is ca. 13–15% for all three mixtures of nitrate and citrate, nitrate–citrate–glycine, and nitrate–citrate–urea. This remaining weight well agrees with the theoretical values expected for the decomposition of Mn(II) nitrate to Mn_3O_4 (15.5%, 13.4%, and 13.8% for nitrate–citrate, nitrate–citrate–glycine, and nitrate–citrate–urea mixtures, respectively).

Moreover, one may argue from comparison of TGA curves for nitrate–citrate and nitrate–citrate–glycine mixtures that in the presence of glycine the decomposition of citrate is slower and is not finished yet below 380 °C (at least under the conditions of TGA measurements). It can be suggested that the intermediate products of the decomposition of citrate (aconate-type anions) are stabilized by the presence of the intermediates of glycine decomposition (amides). Nevertheless, in contrast to pure glycine, nearly no intermediates of glycine thermal decomposition remain above 380 °C in the case of the Mn nitrate–citrate–glycine mixture.

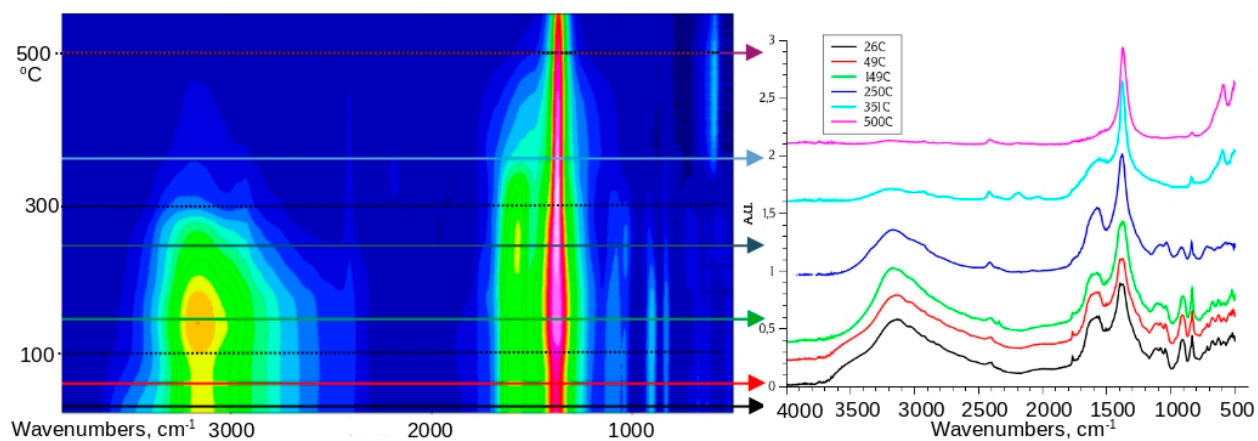
Glycine may substitute water as a ligand in the initial mixture, as indicated by the lower intensity of the water-related $\nu(\text{O-H})$ band. Also, the DRIFT spectra (Figure 5B) show that the dehydration step occurs at a somewhat lower temperature in the presence of glycine: the decrease in the intensity of the $\nu(\text{O-H})$ band is detected already below 100 °C,

and the band nearly disappears at 150 °C. However, after the dehydration step, the DRIFT observations and the TGA behavior are very similar in the case of the presence and absence of glycine in the nitrate–citrate mixture. The decomposition starts with elimination of carbonyl group at temperatures above 150 °C and then a gradual decrease in the intensities of other bands related to citrate above 200 °C.

A



B



C

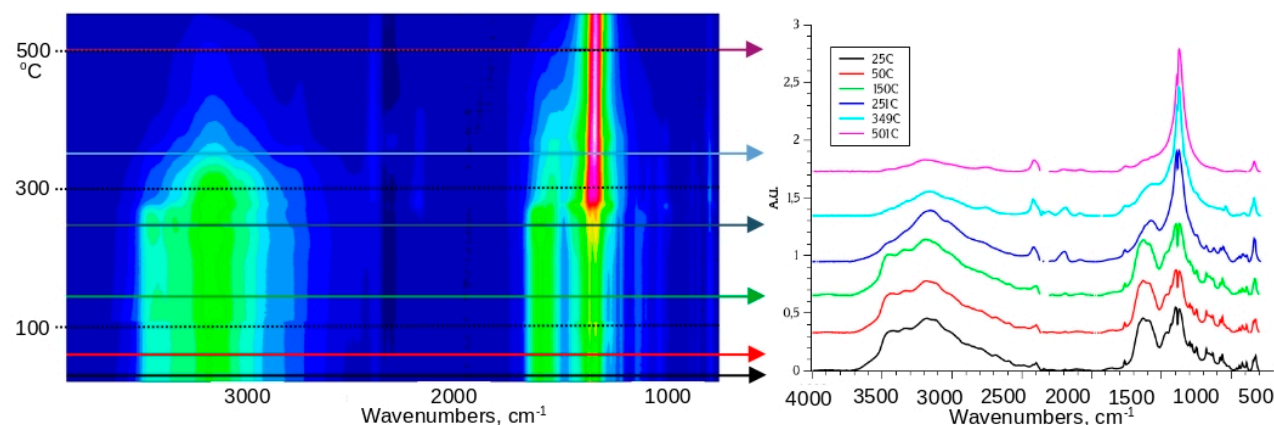


Figure 5. DRIFT spectra of decomposition of SCS mixtures with ammonium citrate: Mn(II) nitrate + ammonium citrate (A), Mn(II) nitrate + ammonium citrate + glycine (B), Mn(II) nitrate + ammonium citrate + urea (C) Arrows indicate the temperature of slice spectra presented on the right side.

The mixture of Mn nitrate–citrate–urea also remains stable with no changes in chemical composition at least up to 150 °C (Figure 5C). Above 200 °C, one starts to observe a decrease in the $\nu(\text{OH})$ band related to the carbonyl of the citrate ligand, similarly to previous cases. Around 250 °C, a strong decrease in other citrate- and nitrate-related bands occurs with the appearance of the band at 2200 cm^{-1} , which can be attributed to $\nu(\text{-C=N})$ or $\nu(\text{-C}\equiv\text{N})$. This band can indicate the formation of intermediates of urea decomposition, such as cyanuric acid, cyanic acid, and cyanamide, as previous detailed studies of urea thermal decomposition have suggested [47,48]. It is noteworthy that, while the intermediates of the decomposition of citrate and urea are still detectable in DRIFT up to ca. 400 °C, the TGA measurements demonstrate that the decomposition is fast finished at ca. 250 °C, and no slow decomposition of intermediates occurs in this case. This discrepancy can be explained by the influence of KBr of DRIFT pellet, allowing more efficient dissipation of heat than in the case of TGA measurements, and hints to the strong exothermic effect of the decomposition of the nitrate–citrate–urea mixture.

3.3.2. Solution Combustion Synthesis with Ammonium Citrate

During SCS synthesis, the dried mixtures of nitrate–citrate, nitrate–citrate–glycine, and nitrate–citrate–urea rapidly decomposes within the first few (1–4) minutes after contacting the heating plate. Within these minutes, one observes melting of the mixture and formation of water vapor, until dried patches are formed. The decomposition reaction starts locally in one or few spots of the dried solid mixture and rapidly propagates within a few or few tens of seconds until the whole solid mixture is converted and no further reaction is observed. However, it is important to emphasize that the propagation of the process is not instantaneous, as in the case of the nitrate–glycine 1:1 mixture, indicating either lower heat effect end/or slower kinetics of the decomposition in the presence of citrate. It is noteworthy that the oxides MnOx-NCG and MnOx-NCU have a smaller average size of crystallites as estimated by XRD in comparison with MnOx-NG oxide, while also smaller SSA (see Table 1). It may indicate that small particles of MnOx-NCG and MnOx-NCU samples are more agglomerated due to slower ignition conditions and, thus, there is less efficient heat evacuation.

As discussed above, the presence of glycine and urea does not strongly influence the first step of decomposition of the Mn citrate complex, which occurs in all cases at nearly the same temperature above 150 °C. The self-propagating process is most probably related to fast and exothermic decomposition of the intermediates of organic decomposition in the presence of Mn.

As SEM images in Figure 6B–D show, the oxides prepared by SCS using ammonium citrate have the morphology similar to the one prepared by the nitrate–glycine method, as described above: the mesoporous structure consists of partially agglomerated oxide nanoparticles. However, there are several important differences related to the utilization of ammonium citrate during the SCS synthesis.

3.4. Electrochemical Properties of Mn Oxides Prepared by SCS

The CV curves of Mn oxide electrodes measured in 1 M NaOH at 10 mV/s are shown in Figure 7A. As mentioned in the Experimental section, the electrode layer contains 70 wt.% of oxide material, and 25 wt.% of carbon black Vulcan XC-72 added for better conductivity of the layer. The specific current of carbon XC-72 in the studied potential region is nearly constant and is below 0.2 A/g. Thus, the currents presented in Figure 7A are predominantly due to the oxide components of electrodes.

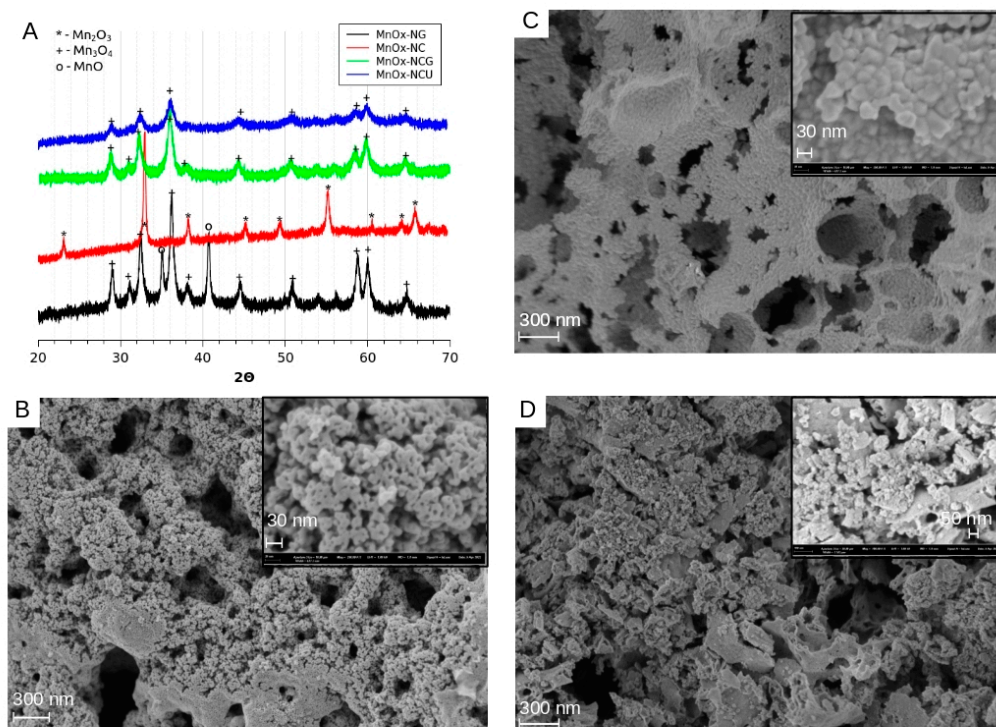
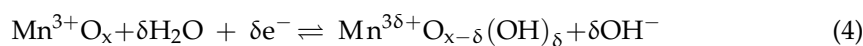


Figure 6. XRD diagrams of Mn oxides synthesized by SCS using nitrate–glycine, nitrate–citrate, and nitrate–citrate–glycine and nitrate–citrate–urea mixtures (A) Typical SEM images of oxides MnOx-NC (B), MnOx-NCG (C), and MnOx-NCU (D).

One detects a clear difference between the electrochemical properties of oxide samples MnOx-NG, MnOx-NCG, and MnOx-NCU, in comparison with oxide MnOx-NC. According to XRD data, the samples MnOx-NCG and MnOx-NCU contain only Mn₃O₄ oxide, which is also a predominant phase in MnOx-NG (with the minor presence of MnO), while MnOx-NC consists of Mn₂O₃ oxide. Thus, the observed difference can be attributed to the different electrochemical properties of two different Mn oxide phases.

Mn₃O₄ hausmannite has a spinel structure with Mn³⁺ cations occupying octahedral and Mn²⁺ occupying tetrahedral sites. Despite the mixed valency of Mn cations in the spinel structure, it was demonstrated [11] that in aqueous solutions the average oxidation state of Mn at the surface is +3 or slightly above. The typical values of the open-circuit potential E_{OCP} of Mn oxide electrodes were typically measured as 0.00–0.10 V vs. NHE, confirming that most Mn at the oxide surface is oxidized to the Mn³⁺ state.

The CV curves in Figure 7A are in agreement with previous studies [8,11] of Mn₃O₄, demonstrating clear pair of peaks around 0.15 V vs. NHE, attributed to the following reversible reaction:



Reaction (4) can propagate further into the bulk of the oxide particles via solid state diffusion of a proton, thus giving rise to pseudocapacitance phenomena via intercalation. The profile of CV curves and galvanostatic discharging curves (Figure 7D) are in qualitative agreement with this mechanism [40]. The analysis of sweep rate dependence of the CV currents by the Dunn method [49] (Figure 8) demonstrated that more than 90% of the CV current recorded at 10 mV/s is proportional to the sweep rate and thus can be attributed to a process that is not limited by solid state diffusion. It confirms that the main charge storage mechanism in the case of Mn₃O₄ particles in 1 M NaOH is a reversible pseudocapacitance via proton intercalation. This high surface-controlled contribution might be

also explained by the nanosizing of the Mn_3O_4 particles and then being referred to as extrinsic pseudocapacitance.

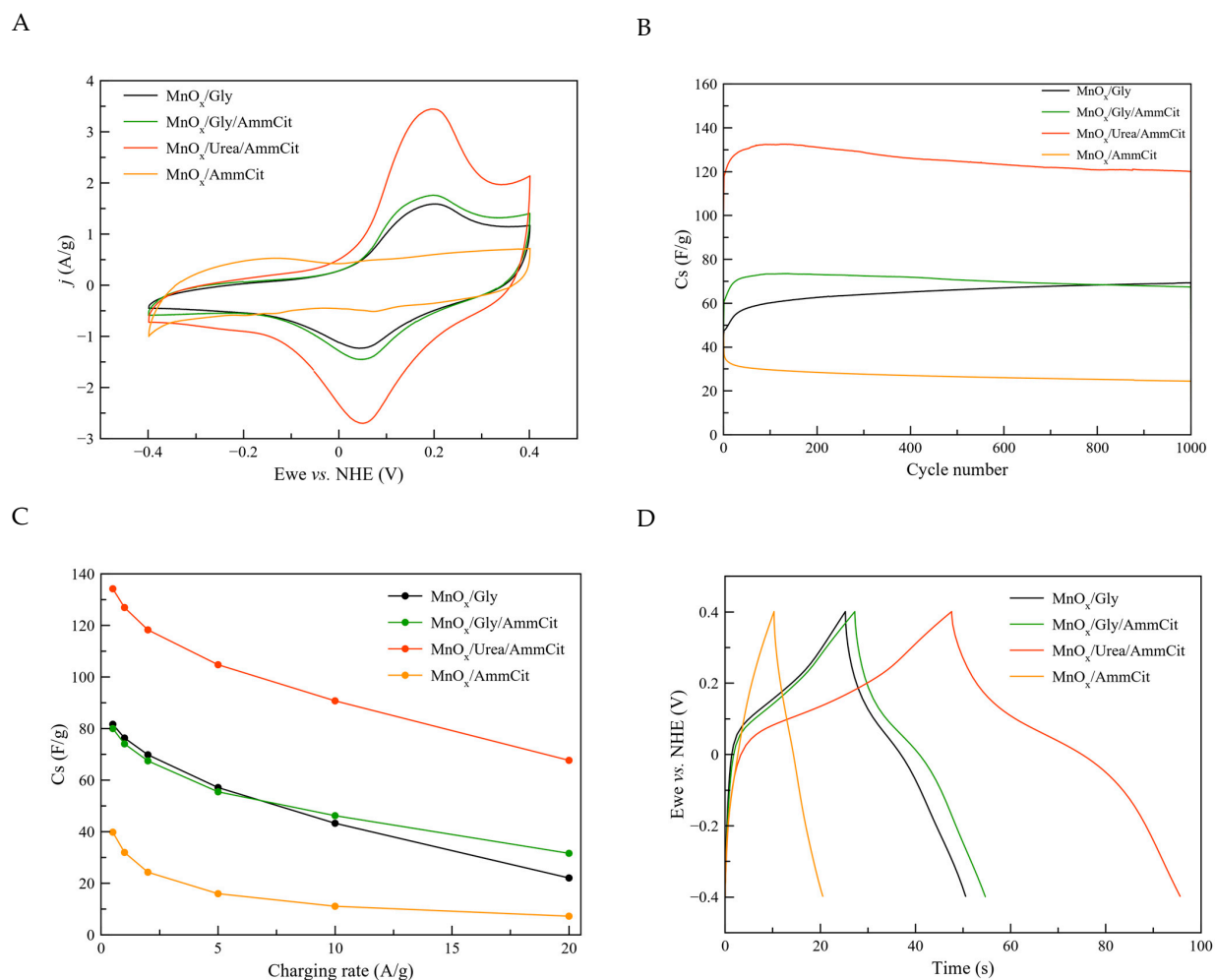


Figure 7. CV curves of MnO_x electrode materials in 1 M NaOH at 20 mV/s (A); dependence of specific capacitance of MnO_x on the charging rate (B); evolution of specific capacitance with galvanostatic charging cycling, measured at 2 A/g (C), chronopotentiograms recorded during the galvanostatic cycling at 2 A/g; GCD curves of MnO_x electrode materials measured at 2 A/g (D).

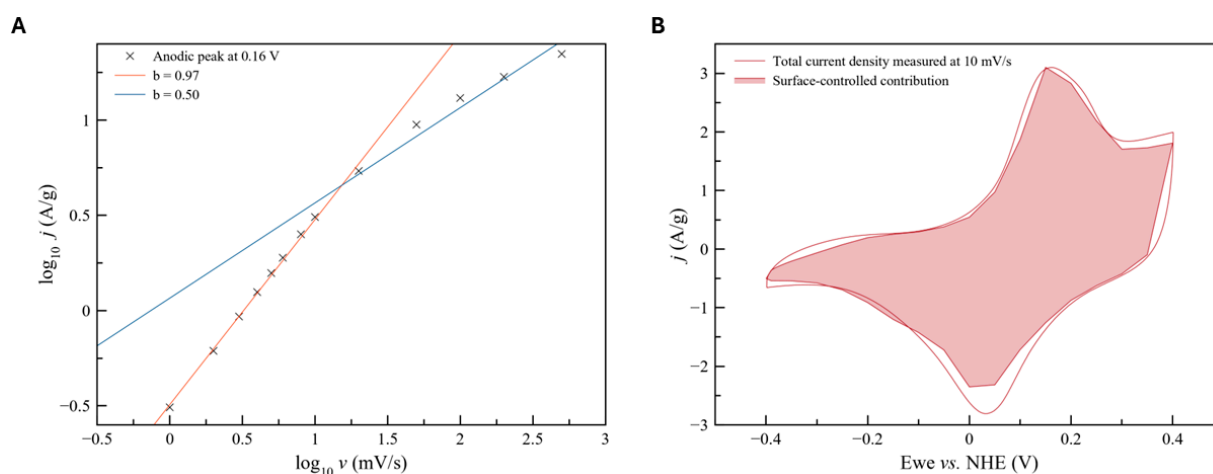


Figure 8. Sweep rate dependence of the CV currents by Dunn method (A) with deconvolution of surface-controlled process for Mn_3O_4 synthesized with urea and ammonium citrate at a 10 mV/s scan rate in 1 M NaOH (B).

In agreement with previous studies [50], the currents corresponding to reaction (4) in the case of Mn_2O_3 oxide are significantly weaker in comparison with Mn_3O_4 oxides. It has been also observed that the peaks related to reaction (4) of Mn_2O_3 are shifted ca. 40 mV to more positive potentials compared with Mn_3O_4 oxide, indicating better stability of Mn^{III} sites of Mn_2O_3 towards oxidation. DFT modeling of water adsorption on the Mn_3O_4 surface [51] demonstrated that the molecular water adsorption is facilitated on Mn^{II} tetrahedral sites due to both their electronic and geometric configuration. Stronger water adsorption on the Mn_3O_4 surface and thermodynamically more facile oxidation of Mn^{III} sites are suggested as the factors explaining much higher currents of reaction (4) detected in the case of Mn_3O_4 oxides compared with Mn_2O_3 .

In contrast to Mn_2O_3 , all Mn_3O_4 oxides demonstrate sufficient stability in 1000 galvanostatic cycles at 2 A/g (Figure 7C). A rapid decrease in charge capacitance of Mn_3O_4 oxides with cycling is a general problem of these oxide electrodes, and is commonly associated to the dissolution of Mn [8,52]. Indeed, we did not detect any changes in the crystallographic structure of Mn oxides after 1000 cycles by post mortem XRD analysis. Thus, we attribute the degradation of capacitance observed for MnOx-NCG and MnOx-NCU samples to dissolution of Mn_3O_4 during galvanostatic cycles. According to the Pourbaix diagram of Mn, at potentials below -0.2 V NHE in 1 M NaOH one may expect reduction of Mn^{III} to Mn^{II} cations and formation of slightly soluble surface hydroxide $\text{Mn}(\text{OH})_2$. This hydroxide is further dissolved in NaOH and can be partially re-deposited upon scan to higher potentials, and partially lost to the bulk of electrolyte. The slow and gradual dissolution of oxide particles may first result in roughening of their surface, which may explain an initial increase in capacitance of MnOx-NCG and MnOx-NCU samples (Figure 7C). However, eventually the loss of oxide material leads to the loss of the capacitance.

This mechanism may also explain the better stability of the MnOx-NG sample, which contains a minor amount of MnO. This oxide is dissolved as $\text{Mn}(\text{OH})_2$ in 1 M NaOH, thus creating a higher local concentration of hydroxide and preventing the dissolution of Mn_3O_4 upon its reduction. Moreover, at potentials above -0.2 V, this hydroxide can be oxidized and re-precipitated on the surface of oxide particles in the form of hydrated Mn oxide, which may contribute to the overall charge capacitance. The precise mechanisms of transformation and degradation of MnOx materials during charging require further investigation, including a thorough analysis of the post mortem structures of the oxides. This will be the focus of our future research.

All oxides demonstrate a decrease in charge capacitance with an increase in charging rate (Figure 7B). This decrease is strongest for Mn_2O_3 oxide (MnOx-NC), while it is approximately the same for all Mn_3O_4 oxides. This decrease can be attributed to limitations related to either slow kinetics of reaction (4) and/or diffusion-related limitations of the propagation of this reaction.

The electrochemical properties of MnOx oxides were studied by electrochemical impedance spectroscopy. The Figure 9 shows the Nyquist and Bode plots (for phase angle) of four studied oxide samples measured at 0.00 V Hg/HgO. At high frequencies, the phase angle of impedance is close to 0° , indicating that the impedance is predominantly by the resistance of an electrolyte. As the frequency decreases, as expected for capacitive materials, the phase angle is increasing to the values close to 90° . The transition between resistive and capacitive behavior is smooth and uniform, indicating the influence of the porosity of the electrode layer and dispersion of sizes of pores and particles. These factors results in non-uniform conditions of polarization of the interface inside the pores. The ideal capacitive behavior is not observed, even at low frequencies. This can be related to two factors. The impedance of the pseudocapacitance reaction can be partially controlled by the rate of charge transfer kinetics, which has a resistive contribution to the impedance. Second, the

dispersion of the accessibility of the interface inside the pores of the electrode layer results in the behavior best described by the constant phase element (CPE) with the power $a < 1$, also resulting in the lower-phase angle. For all samples, an increase in the phase angle with frequency decrease is not uniform, demonstrating plateaus and, in some cases, local maximums. Such behavior is related to the complex character of the impedance, containing the contributions from double-layer charging and pseudocapacitance reaction, and to the influence of the porous structure of the electrode layer. It is more informative in this case to analyze the behavior of the complex interfacial capacitance, C_z , calculated as follows:

$$C_z = \frac{1}{m} \frac{1}{\omega(Z-R_\Omega)};$$

$$Re(C_z) = \frac{1}{m} \frac{-Im(Z)}{\omega|Z-R_\Omega|^2};$$

$$Im(C_z) = \frac{1}{m} \frac{Re(Z-R_\Omega)}{\omega|Z-R_\Omega|^2}.$$
(5)

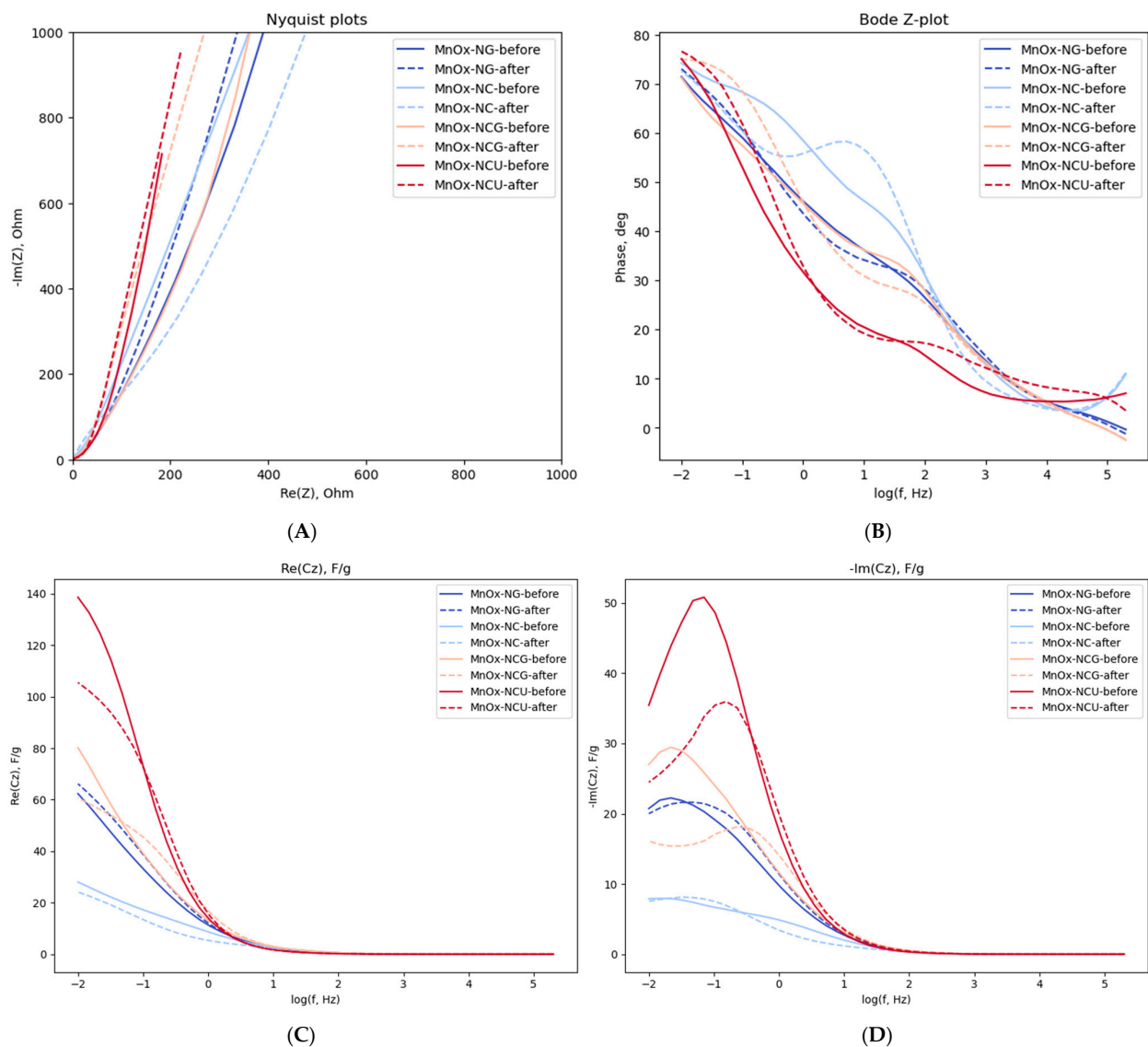


Figure 9. Electrochemical impedance data for 4 studied oxide samples, measured in 1 M NaOH at 0.00 V Hg/HgO. Solid curves correspond to the initial state of the electrode, and dashed curves correspond to the data measured after 1000 galvanostatic charging cycles. The data shown as Nyquist plots (A), Bode plots showing impedance phase angle (B), real part (C) and imaginary part (D) of interfacial complex capacitance.

In equation above, Z is the measured electrochemical impedance, R_{Ω} is a serial electrolyte resistance outside of the electrode deposit, m is the mass of the electrode deposit, and ω is an angular frequency. $Re(C_z)$ is a measurable interfacial capacitance, proportional to the surface specific capacitance and interfacial surface area. It is decreasing with an increase in frequency due to (i) slowing down the charging of interfacial capacitance due to the influence of resistive components, such as interfacial charge transfer resistance, and the resistance of the electrolyte inside the pores, and (ii) shorter penetration of potential modulation into the porous electrode deposit. The imaginary component $Im(C_z)$ indicates the loss of capacitance due to the influence of resistive components. Its maximum corresponds to the reciprocal of the characteristic response time of the impedance components, while its width is related to the dispersion in the polarizability of the interface [53].

In agreement with the data from CV and galvanostatic cycling, the interfacial capacitance decreases in the sequence $MnOx-NCU > MnOx-NCG > MnOx-NG \gg MnOx-NC$ (Figure 9C). It is noteworthy that $MnOx-NCU$ also shows the fastest response to the potential modulation, as indicated by the position of the $Im(C_z)$ peak at the highest frequencies compared with other oxides. It may be tentatively attributed to either a faster charge transfer during the reaction (4) or a more open and accessible porous structure resulting from the smaller resistance of the electrolyte inside the pores. The exact attribution of the behavior of $-Im(C_z)$ plots requires analysis of the dependence on the potential and is beyond the point of the present manuscript.

Figure 9 also shows how the impedance of the oxide electrode sample changes after 1000 galvanostatic cycles of charging at 2 A/g (dashed curves). For all samples, except $MnOx-NG$, a loss of interfacial capacitance, as measured by $Re(C_z)$, Figure 9C, is observed, while a slight increase in capacitance is detected for $MnOx-NG$. These observations are in accordance with the data of Figure 7C on the evolution of the capacitance with the number of galvanostatic cycles. The peaks of the $-Im(C_z)$ plots shift to higher frequencies after 1000 cycles for all samples, and especially for $MnOx-NCG$ and $MnOx-NCU$. It can be interpreted as either a faster charge transfer or a smaller electrolyte resistance in pores resulting from the galvanostatic cycling. Thus, the main mechanism of the loss of capacitance cannot be attributed to a decrease in the surface-specific charge capacitance, but rather to the decrease in the surface area available for charge storage, resulting from the dissolution of the material.

4. Discussion

4.1. Nitrate–Glycine Synthesis

Concerning the thermal decomposition study via TD-DRIFTS and TGA analyses of dried nitrate, glycine and their mutual mixture with a $\varphi = 1.0$ ratio, a given number of suggestions for the SCS mechanism are given as follows:

- During slow evaporation of the solvent from the nitrate and glycine mixed solution, the glycine complex of Mn(II) is formed, either $[Mn(gly)(H_2O)_2](NO_3)_2$ or $[Mn(gly)(H_2O)_4](NO_3)_2$. Formation of this complex ensures fine and uniform mixing of the components of the SCS mixture.
- The glycine complexes of Mn(II) are thermodynamically less stable than complexes of other transition metals [31,32] and easily decompose upon heating [18]. The decomposition of this complex follows up its partial dehydration, and occurs at a temperature of 160–170 °C, which is below the decomposition of pure glycine (220 °C). It has been previously reported that decomposition of a dried Mn nitrate–glycine mixture also occurs at a lower temperature compared with pure glycine under an inert atmosphere [26].
- In comparison with a decomposition of pure nitrate and glycine, the first step of the decomposition of the dried mixture is fast, and results in the formation of a

large number of gas products. One may assume the “autocatalytic” mechanism of glycine/nitrate decomposition with the formation of the glycine complex of Mn(II) as a catalytic intermediate. The fast kinetics of glycine–nitrate decomposition may be an indication of the lowering of activation energy of this reaction, which is otherwise relatively high for both nitrate (210 kJ/mol) and glycine (155 kJ/mol) decompositions.

The observation of the SCS reaction also supports the assumption of the formation of the complex intermediate. Indeed, the dried mixture of components reacts instantaneously within the first minute of the contact with the heating plate at 350 °C and without any visible sign of phase transition. The only observation upon heating of the dried mixture before ignition is formation of water vapor due to dehydration of the complex. No liquid phase due to melting of $\text{Mn}(\text{NO}_3)_2$ (melting point $t_f^\circ = 37^\circ\text{C}$) is observed.

4.2. Analysis of the Products of SCS with Nitrate–Glycine Mixture

Considering slow drying of the precursor mixture, and an instantaneous character of the SCS process, one may expect uniform reaction conditions and formation of a single oxide phase. Nevertheless, for all nitrate + glycine mixtures, we always produced a mixture of oxides (see Table 1). In particular, for all $\varphi \geq 1$, a mixture of Mn_3O_4 (predominant phase) and MnO (minor component) was formed, in agreement with previous studies [26]. The formation of a mixture of products can be related to the following:

- The formation of a mixture of oxides can be attributed to the partial reduction of Mn_3O_4 to MnO, indicating a high temperature generated during the SCS decomposition reaction: at $p(\text{O}_2) = 1$ bar, MnO formation is detected only above 820 °C (Figure 1B). MnO remains a minor product due to the effective evacuation of generated heat by the formed gaseous products. However, if Mn_2O_3 or Mn_3O_4 oxide reduction to MnO is the main source of this oxide, one would expect its systematically higher content formed with a higher φ value (due to a higher reaction temperature), which was not experimentally observed.
- The alternative explanation of the formation of MnO as an SCS product is the precipitation of $\text{Mn}(\text{OH})_2$ hydroxide due to the hydrolysis of Mn(II) nitrate during the solution evaporation. The pH of the solution of Mn(II) nitrate is slightly acidic (pH = 4.6), both in the absence and in the presence of glycine, and thus no precipitation of $\text{Mn}(\text{OH})_2$ ($\text{p}K_b = 12.7$) is expected from the nitrate solution. However, Mn(II) hydroxide may be precipitated during the evaporation of the solvent due its much lower solubility compared with nitrate (0.34 mg/100 mL and 118 g/100 mL, respectively). The precipitated $\text{Mn}(\text{OH})_2$ hydroxide is then decomposed during the SCS reaction to MnO. The latter is not oxidized to higher oxides due to the oxygen-lean atmosphere within the SCS reaction.

It must be borne in mind that, in addition to the composition of the initial SCS mixture and φ ratio, other SCS conditions may strongly effect the T_{ad} and p_{O_2} . Nitrate–glycine synthesis with very fast evaporation of solvent (in less than 20 min) on a heating plate resulted in formation of the same $\epsilon\text{-MnO}_2$ oxide for both $\varphi = 0.5$, and $\varphi = 2.0$ [54]. On the other hand, the main product of nitrate–glycine SCS ($\varphi = 1.5$) with fast solvent evaporation in an oven at 500 °C is Mn_3O_4 , and when slower evaporation is performed at a lower temperature of 350 °C, the products are Mn_2O_3 and MnO_2 [55]. Thus, the temperature ramp, the rate of evaporation, and the mode of heating (bottom heating on a heating plate or all-around inside an oven) are also the important conditions to bear in mind. It may be speculated that the slower evaporation of the solvent favors the hydrolysis of the Mn precursor salt and precipitation of Mn hydroxide, resulting in the mixture of final oxide products.

4.3. SCS Synthesis with Ammonium Citrate: Nitrate–Citrate, Nitrate–Citrate–Glycine, and Nitrate–Citrate–Urea Mixtures

Three main points are listed below concerning the obtained manganese oxide particles and their differences in structural characteristics from nitrate–citrate, nitrate–citrate–glycine, and nitrate–citrate–urea mixtures:

- In all three cases (Mn nitrate–citrate, nitrate–citrate–glycine, and nitrate–citrate–urea) only one crystalline oxide phase was detected, despite slower kinetics of decomposition and less uniform conditions of reaction propagation, compared with nitrate–glycine synthesis. This observation supports the assumption that the main source of inhomogeneity in the final products of SCS is the formation of various forms of Mn precursors, such as metal complexes, dried salt, and hydroxide, during the slow step of solvent evaporation. In the presence of citrate in the solution, Mn forms a strong and stable complex with citrate ligands, which uniformly precipitates after solvent evaporation.
- In the case of ammonium citrate being the only fuel of the SCS process, the only product of the reaction is Mn_2O_3 (Figure 6A), while, in the presence of glycine and urea in the mixture, only Mn_3O_4 is formed. It can be argued that the presence of glycine or urea allows a higher temperature to be reached during the SCS reaction; alternatively, the decomposition of the intermediates of glycine or urea decomposition consumes oxygen, resulting in a lower local partial pressure, $p(\text{O}_2)$. Both factors favor the formation of a more reduced oxide, namely Mn_3O_4 .
- XRD estimation of crystallite size, measurements of specific surface area, and SEM images point to a smaller particle size in the case of nitrate–citrate–urea compared with the nitrate–citrate–glycine mixture. We attribute this effect to faster kinetics of the second step of decomposition of the nitrate–citrate–urea mixture, in which case the formation of a larger number of smaller particles is favored, while particles are less sintered due to a shorter reaction time. In both nitrate–citrate–glycine and nitrate–citrate–urea synthesis, the particles are more sintered than in the case of nitrate–glycine synthesis, due to much faster reaction propagation and heat dissipation in the latter case.

4.4. Electrochemical Properties of Mn Oxides Prepared by SCS

The ensemble of electrochemical and physicochemical data allows to give the following tentative interpretation of the difference in structure, electrochemical properties, and cycling behavior of the studied samples.

- The MnOx-NG sample consists of relatively large (ca. 20 nm) particles, which are not strongly sintered because of the explosive character of the SCS reaction. The explosive character of the SCS process is related to the formation of a weak complex between Mn(II) nitrate and glycine, which is easily decomposed upon heating and provides a significant exothermic effect for instantaneous self-propagation of the reaction. The final oxide product contains ca. 20%mol. of MnO and 80% of Mn_3O_4 , and the presence of MnO is related to the hydrolysis of Mn nitrate during the slow evaporation of solvent before the SCS reaction. The MnOx-NG electrode shows moderate charge capacitance (70 F/g at 2 A/g discharge) and a very stable performance. MnO oxide is not stable in 1 M NaOH and forms hydroxide, which does not contribute to the charge capacitance; however, its presence allows the prevention of dissolution of Mn_3O_4 oxide upon reduction in the form of Mn hydroxide, which is the main mechanism of this material degradation. The capacitance can be further significantly improved by forming a composite with carbon materials, as it is demonstrated in previous studies [8].

- The MnO_x-NC sample consists of Mn₂O₃ oxide particles of ca. 20 nm, slightly sintered. Citrate forms a stronger complex with Mn(II), and its decomposition is not sufficiently exothermic to generate a temperature sufficient for Mn₃O₄ formation, which requires ca. 950 °C at $p(\text{O}_2) = 0.3$ bar. MnO_x-NC oxide demonstrates a low charge capacitance in 1 M NaOH (initially 22 F/g at 2 A/g), which is fast degrading upon galvanostatic cycling. The degradation cannot be explained only by possible dissolution of Mn oxide, but suggests changes in surface structure or composition, which may result in a strong increase in contact interparticle resistance.
- Addition of an equimolar amount of a fuel, either glycine (MnO_x-NCG) or urea (MnO_x-NCU), to the Mn(II) nitrate–ammonium citrate mixture allows an increase in the exothermic effect of the reaction and Mn₃O₄ oxide nanoparticles to be obtained. Formation of MnO is suppressed by the presence of citrate. The SCS reaction in these cases is slower than in the case of MnO_x-NG, and takes a few seconds. The reaction is slower in the case of the nitrate–citrate–glycine mixture in comparison with the nitrate–citrate–urea mixture, which is explained by possible interactions between the intermediates of citrate and glycine decomposition. The slower rate of reaction results in more sintered particles in comparison with MnO_x-NG synthesis. Nevertheless, MnO_x-NCU oxide demonstrates the highest charge capacitance due to strong and fast pseudocapacitance phenomena (130 F/g at 2 A/g). The high capacitance of this oxide can be explained by its relatively high SSA, providing a fast charging rate and moderate sintering of particles, decreasing the interparticle contact resistance. Upon cycling, the capacitance of both MnO_x-NCG and MnO_x-NCU, after the initial increase within the first 100 cycles, slowly decays, resulting from the dissolution of Mn₃O₄ upon reduction in the form of Mn(II) hydroxide. Further study of the mechanism of dissolution of Mn₃O₄ particles upon their electrochemical performance is needed to develop the strategy to avoid their degradation.

5. Conclusions

Mesoporous manganese oxide materials have been synthesized by solution combustion synthesis (SCS) and tested for supercapacitor application. The structure and composition of oxides strongly depend on the choice of initial components of the SCS mixture. In particular, the appearance of a mixture of oxides, namely MnO and Mn₃O₄, for a fuel-rich nitrate–glycine mixture (MnO_x-NG-1-1, MnO_x-NG-1-1.25, and MnO_x-NG-1.5) is explained by a partial hydrolysis of manganese salt during slow evaporation of the solvent and formation of Mn(II) hydroxide. The ATR-FTIRS and DRIFTS data point to the formation of a glycine-complex of Mn(II) in solution with glycine; this complex is weak and does not prevent the hydrolysis. Its decomposition is fast and exothermic, resulting in instantaneous propagation of the combustion reaction, and relatively weak sintering of oxide particles of the final product. The addition of ammonium citrate leads to the formation of a strong complex or mixture of complexes (e.g., mono- and bidentate complexes) with Mn(II). The formation of a citrate complex prevents the hydrolysis of Mn(II) salt, thus providing only one crystalline oxide phase in the final product. In the absence of another fuel, i.e., from Mn(II) nitrate–ammonium citrate solution (MnO_x-NC), only Mn₂O₃ is formed due to the low temperature generated from the combustion reaction. If an equimolar quantity of another fuel, namely glycine or urea, is added, Mn₃O₄ is the only oxide product (MnO_x-NCG and MnO_x-NCU, correspondingly). The presence of a fuel component does not noticeably affect the formation of the Mn(II) citrate complex, but provides a higher temperature during the combustion reaction. Decomposition of the citrate complex of Mn(II) is slower compared with the glycine complex, and, thus, the propagation of the combustion reaction is also slower, resulting in a longer reaction time

and stronger sintering of resulting oxides. Urea is a more efficient fuel than glycine for Mn citrate decomposition, resulting in a shorter reaction time and weaker sintering of the final oxide.

The charge capacitance of oxides decreases in the sequence $\text{MnO}_x\text{-NCU} > \text{MnO}_x\text{-NCG} \approx \text{MnO}_x\text{-NG} \gg \text{MnO}_x\text{-NC}$. The weak capacitance of $\text{MnO}_x\text{-NC}$ oxide is related to the properties of Mn_2O_3 , which is an oxide phase in the case of this sample, contrary to Mn_3O_4 , which is the only or predominant oxide phase in the case of the three other samples. The oxide $\text{MnO}_x\text{-NCU}$ demonstrates the highest charge capacitance in 1 M NaOH (130 F/g at 2 A/g charging rate with 0.75 mg/cm² loading). The capacitance of both $\text{MnO}_x\text{-NCG}$ and $\text{MnO}_x\text{-NCU}$ starts to slowly decrease after ca. 100 charging cycles, related to the dissolution of oxides. In contrast to these samples, the capacitance of $\text{MnO}_x\text{-NG}$ oxide increases continuously within at least 1000 cycles of charging, which is tentatively explained by the stabilizing effect of the presence of MnO in this case.

Supplementary Materials: The following supporting information can be downloaded at: <https://www.mdpi.com/article/10.3390/batteries11020039/s1>. Table S1. Decomposition reaction that may occur in the course of SCS synthesis with $\text{Mn}(\text{NO}_3)_2$ and various fuels. Table S2. Overview of studies of SCS synthesis of Mn oxides. Figure S1. N₂ isotherm of the MnO_x /glycine sample. Figure S2. N₂ isotherm of the MnO_x /glycine samples with different φ ratios. Figure S3. N₂ isotherm of the MnO_x /urea sample. Figure S4. N₂ isotherm of MnO_x /glycine–ammonium citrate. Figure S5. MnO_x /urea–ammonium citrate. Figure S6. The CV curves for $\text{MnO}_x\text{-NG}$ (A) and $\text{MnO}_x\text{-NCU}$ (B) samples in 1 M NaOH recorded at different sweep rates. The CV curves containing only the current contribution linear-to-sweep rate are depicted below for $\text{MnO}_x\text{-NG}$ (C) and $\text{MnO}_x\text{-NCU}$ (D) as a filled area figure.

Author Contributions: Conceptualization, S.N.P.; methodology, S.N.P.; validation, S.N.P. and T.K.; experimental work, T.K. and S.S.; resources, T.K. and S.S.; writing—original draft preparation, S.N.P. and T.K.; writing—review and editing, S.N.P. and T.K.; supervision, S.N.P.; project administration, S.N.P.; funding acquisition, S.N.P. All authors have read and agreed to the published version of the manuscript.

Funding: This research was funded by the INFINE ANR (France) project ANR-21-CE08-0025-01.

Data Availability Statement: The raw experimental data for the results discussed in the present paper can be provided by the authors of the manuscript on demand.

Acknowledgments: The authors are grateful to the staff of ICPEES for performing and assisting in the materials characterization. Special thanks are given to Corinne Petit (ICPEES) for helping with DRIFTS conceptualization.

Conflicts of Interest: The authors declare no conflicts of interest.

References

1. Tarascon, J.M.; Armand, M. Issues and Challenges Facing Rechargeable Lithium Batteries. *Nature* **2001**, *414*, 359–367. [[CrossRef](#)] [[PubMed](#)]
2. Poizot, P.; Laruelle, S.; Grugeon, S.; Dupont, L.; Tarascon, J.M. Nano-Sized Transition-Metal Oxides as Negative-Electrode Materials for Lithium-Ion Batteries. *Nature* **2000**, *407*, 496–499. [[CrossRef](#)] [[PubMed](#)]
3. Lin, Z.; Goikolea, E.; Balducci, A.; Naoi, K.; Taberna, P.L.; Salanne, M.; Yushin, G.; Simon, P. Materials for Supercapacitors: When Li-Ion Battery Power Is Not Enough. *Mater. Today* **2018**, *21*, 419–436. [[CrossRef](#)]
4. Thackeray, M.M. Manganese Oxides for Lithium Batteries. *Prog. Solid State Chem.* **1997**, *25*, 1–71. [[CrossRef](#)]
5. Thackeray, M.M. Exploiting the Spinel Structure for Li-Ion Battery Applications: A Tribute to John B. Goodenough. *Adv. Energy Mater.* **2021**, *11*, 2001117. [[CrossRef](#)]
6. Shah, H.U.; Wang, F.; Toufiq, A.M.; Khattak, A.M.; Iqbal, A.; Ghazi, Z.A.; Ali, S.; Li, X.; Wang, Z. Electrochemical Properties of Single-Crystalline Mn_3O_4 Nanostructures and Their Capacitive Performance in Basic Electrolyte. *Int. J. Electrochem. Sci.* **2016**, *11*, 8155–8162. [[CrossRef](#)]

7. Shah, H.U.; Wang, F.; Toufiq, A.M.; Ali, S.; Khan, Z.U.H.; Li, Y.; Hu, J.; He, K. Electrochemical Properties of Controlled Size Mn_3O_4 Nanoparticles for Supercapacitor Applications. *J. Nanosci. Nanotechnol.* **2018**, *18*, 719–724. [[CrossRef](#)]
8. Kerangueven, G.; Faye, J.; Royer, S.; Pronkin, S.N. Electrochemical Properties and Capacitance of Hausmannite Mn_3O_4 –Carbon Composite Synthesized by in Situ Autocombustion Method. *Electrochim. Acta* **2016**, *222*, 755–764. [[CrossRef](#)]
9. Wang, J.-G.; Jin, D.; Zhou, R.; Li, X.; Liu, X.; Shen, C.; Xie, K.; Li, B.; Kang, F.; Wei, B. Highly Flexible Graphene/ Mn_3O_4 Nanocomposite Membrane as Advanced Anodes for Li-Ion Batteries. *ACS Nano* **2016**, *10*, 6227–6234. [[CrossRef](#)]
10. Wang, H.; Cui, L.-F.; Yang, Y.; Sanchez Casalongue, H.; Robinson, J.T.; Liang, Y.; Cui, Y.; Dai, H. Mn_3O_4 –Graphene Hybrid as a High-Capacity Anode Material for Lithium Ion Batteries. *J. Am. Chem. Soc.* **2010**, *132*, 13978–13980. [[CrossRef](#)]
11. Dosaev, K.A.; Istomin, S.Y.; Strebkov, D.A.; Tsirlina, G.A.; Antipov, E.V.; Savinova, E.R. AMn_2O_4 Spinel (A–Li, Mg, Mn, Cd) as ORR Catalysts: The Role of Mn Coordination and Oxidation State in the Catalytic Activity and Their Propensity to Degradation. *Electrochim. Acta* **2022**, *428*, 140923. [[CrossRef](#)]
12. Patil, K.C.; Aruna, S.T.; Mimani, T. Combustion Synthesis: An Update. *Curr. Opin. Solid State Mater. Sci.* **2002**, *6*, 507–512. [[CrossRef](#)]
13. Chick, L.A.; Pederson, L.R.; Maupin, G.D.; Bates, J.L.; Thomas, L.E.; Exarhos, G.J. Glycine-Nitrate Combustion Synthesis of Oxide Ceramic Powders. *Mater. Lett.* **1990**, *10*, 6–12. [[CrossRef](#)]
14. Kingsley, J.J.; Suresh, K.; Patil, K.C. Combustion Synthesis of Fine-Particle Metal Aluminates. *J. Mater. Sci.* **1990**, *25*, 1305–1312. [[CrossRef](#)]
15. Manoharan, S.S.; Patil, K.C. Combustion Synthesis of Metal Chromite Powders. *J. Am. Ceram. Soc.* **1992**, *75*, 1012–1015. [[CrossRef](#)]
16. Arul Dhas, N.; Patil, K.C. Combustion Synthesis and Properties of Fine Particle Spinel Manganites. *J. Solid State Chem.* **1993**, *102*, 440–445. [[CrossRef](#)]
17. Varma, A.; Mukasyan, A.S.; Rogachev, A.S.; Manukyan, K.V. Solution Combustion Synthesis of Nanoscale Materials. *Chem. Rev.* **2016**, *116*, 14493–14586. [[CrossRef](#)]
18. Mrozek, R.; Rz, Z. Thermal Analysis of Manganese(II) Complexes With Glycine. *J. Therm. Anal. Calorim.* **2001**, *63*, 839–846. [[CrossRef](#)]
19. Khaliullin, S.M.; Zhuravlev, V.D.; Bamburov, V.G. Solution-Combustion Synthesis of Oxide Nanoparticles from Nitrate Solutions Containing Glycine and Urea: Thermodynamic Aspects. *Int. J. Self-Propag. High-Temp. Synth.* **2016**, *25*, 139–148. [[CrossRef](#)]
20. Vratny, F. Infrared Spectra of Metal Nitrates. *Appl. Spectrosc.* **1959**, *13*, 59–70. [[CrossRef](#)]
21. Laulich, I.; Pinchas, S.; Samuel, D.; Wasserman, I. The Infrared Absorption Spectrum of Oxygen-18-Labeled Glycine. *J. Phys. Chem.* **1966**, *70*, 2719–2725. [[CrossRef](#)] [[PubMed](#)]
22. Kumar, S.; Rai, A.K.; Singh, V.B.; Rai, S.B. Vibrational Spectrum of Glycine Molecule. *Spectrochim. Acta Part A Mol. Biomol. Spectrosc.* **2005**, *61*, 2741–2746. [[CrossRef](#)] [[PubMed](#)]
23. Popov, D.; Herak, R.; Prelesnik, B.; Ribar, B. The Crystal Structure of Manganese Nitrate Tetrahydrate $Mn(NO_3)_2 \cdot 4H_2O$. *Z. Für Krist. Cryst. Mater.* **1973**, *137*, 280–289. [[CrossRef](#)]
24. Nakamoto, K. Applications in Coordination Chemistry. In *Infrared and Raman Spectra of Inorganic and Coordination Compounds*; John Wiley & Sons, Ltd.: Hoboken, NJ, USA, 2008; pp. 1–273, ISBN 978-0-470-40588-8.
25. Devereux, M.; Jackman, M.; McCann, M.; Casey, M. Preparation and Catalase-Type Activity of Manganese(II) Amino Acid Complexes. *Polyhedron* **1998**, *17*, 153–158. [[CrossRef](#)]
26. Komova, O.V.; Mukha, S.A.; Ozerova, A.M.; Odegova, G.V.; Simagina, V.I.; Bulavchenko, O.A.; Ishchenko, A.V.; Netskina, O.V. The Formation of Perovskite during the Combustion of an Energy-Rich Glycine–Nitrate Precursor. *Materials* **2020**, *13*, 5091. [[CrossRef](#)]
27. Hegedüs, A.J.; Horkay, K.; Székely, M.; Stefánai, W. Thermogravimetrische Untersuchung der Mangan(II)-oxid-Pyrolyse. *Mikrochim. Acta* **1966**, *54*, 853–864. [[CrossRef](#)]
28. Greenberg, J.; Hallgren, L.J. Infrared Absorption Spectra of Alkali Metal Nitrates and Nitrites above and below the Melting Point. *J. Chem. Phys.* **1960**, *33*, 900–902. [[CrossRef](#)]
29. Gallagher, P.K.; Schrey, F.; Prescott, B. The Thermal Decomposition of Aqueous Manganese (II) Nitrate Solution. *Thermochim. Acta* **1971**, *2*, 405–412. [[CrossRef](#)]
30. Huang, M.; Lv, S.; Zhou, C. Thermal Decomposition Kinetics of Glycine in Nitrogen Atmosphere. *Thermochim. Acta* **2013**, *552*, 60–64. [[CrossRef](#)]
31. Casale, A.; De Robertis, A.; De Stefano, C.; Gianguzza, A.; Patanè, G.; Rigano, C.; Sammartano, S. Thermodynamic Parameters for the Formation of Glycine Complexes with Magnesium(II), Calcium(II), Lead(II), Manganese(II), Cobalt(II), Nickel(II), Zinc(II) and Cadmium(II) at Different Temperatures and Ionic Strengths, with Particular Reference to Natural Fluid Conditions. *Thermochim. Acta* **1995**, *255*, 109–141. [[CrossRef](#)]
32. Yamashita, H.; Nozaki, T.; Fukuda, Y.; Kabata, T. A Polarographic Study of the Glycine Complexes of Copper(II), Lead(II), Cadmium(II), and Manganese(II). *Bull. Chem. Soc. Jpn.* **1991**, *64*, 697–698. [[CrossRef](#)]

33. Wen, W.; Wu, J.-M. Nanomaterials via Solution Combustion Synthesis: A Step Nearer to Controllability. *RSC Adv.* **2014**, *4*, 58090–58100. [[CrossRef](#)]
34. Fritsch, S.; Navrotsky, A. Thermodynamic Properties of Manganese Oxides. *J. Am. Ceram. Soc.* **1996**, *79*, 1761–1768. [[CrossRef](#)]
35. Matzapetakis, M.; Karligiano, N.; Bino, A.; Dakanali, M.; Raptopoulou, C.P.; Tangoulis, V.; Terzis, A.; Giapintzakis, J.; Salifoglou, A. Manganese Citrate Chemistry: Syntheses, Spectroscopic Studies, and Structural Characterizations of Novel Mononuclear, Water-Soluble Manganese Citrate Complexes. *Inorg. Chem.* **2000**, *39*, 4044–4051. [[CrossRef](#)]
36. Deng, Y.F.; Zhou, Z.H. Manganese Citrate Complexes: Syntheses, Crystal Structures and Thermal Properties. *J. Coord. Chem.* **2009**, *62*, 778–788. [[CrossRef](#)]
37. Strouse, J.; Layten, S.W.; Strouse, C.E. Structural Studies of Transition Metal Complexes of Triionized and Tetraionized Citrate. Models for the Coordination of the Citrate Ion to Transition Metal Ions in Solution and at the Active Site of Aconitase. *J. Am. Chem. Soc.* **1977**, *99*, 562–572. [[CrossRef](#)]
38. Wang, W.; Zhang, X.; Chen, F.; Ma, C.; Chen, C.; Liu, Q.; Liao, D.; Li, L. Homo- and Hetero-Metallic Manganese Citrate Complexes: Syntheses, Crystal Structures and Magnetic Properties. *Polyhedron* **2005**, *24*, 1656–1668. [[CrossRef](#)]
39. Feick, G.; Hainer, R.M. On the Thermal Decomposition of Ammonium Nitrate. Temperatures and Reaction Rate. *J. Am. Chem. Soc.* **1954**, *698*, 5860–5863. [[CrossRef](#)]
40. Chaturvedi, S.; Dave, P.N. Review on Thermal Decomposition of Ammonium Nitrate. *J. Energetic Mater.* **2013**, *31*, 1–26. [[CrossRef](#)]
41. Babrauskas, V.; Leggett, D. Thermal Decomposition of Ammonium Nitrate. *Fire Mater.* **2019**, *44*, 1–19. [[CrossRef](#)]
42. Grzybowski, A.K.; Tate, S.S.; Datta, S.P. Magnesium and Manganese Complexes of Citric and Isocitric Acids. *J. Chem. Soc. A* **1970**, 241–245. [[CrossRef](#)]
43. Wheatley, A.M.; Kaduk, J.A. Crystal Structures of Ammonium Citrates. *Powder Diffr.* **2019**, *34*, 35–43. [[CrossRef](#)]
44. Barbooti, M.M.; Dhoab, A.-S.A. Thermal Decomposition of Citric Acid. *Thermochim. Acta* **1986**, *98*, 119–126. [[CrossRef](#)]
45. Wyrzykowski, D.; Hebanowska, E.; Nowak-Wicz, G.; Makowski, M.; Chmurzyński, L. Thermal Behaviour of Citric Acid and Isomeric Aconitic Acids. *J. Therm. Anal. Calorim.* **2011**, *104*, 731–735. [[CrossRef](#)]
46. Valletta, R.M.; Pliskin, W.A. Preparation and Characterization of Manganese Oxide Thin Films. *J. Electrochem. Soc.* **1967**, *114*, 944–947. [[CrossRef](#)]
47. Paleckiene, R.; Sviklas, A.; Slinksiene, R. Reaction of Urea with Citric Acid. *Russ. J. Appl. Chem.* **2005**, *78*, 1651–1655. [[CrossRef](#)]
48. Schaber, P.M.; Colson, J.; Higgins, S.; Thielen, D.; Anspach, B.; Brauer, J. Thermal Decomposition (Pyrolysis) of Urea in an Open Reaction Vessel. *Thermochim. Acta* **2004**, *424*, 131–142. [[CrossRef](#)]
49. Fleischmann, S.; Mitchell, J.B.; Wang, R.; Zhan, C.; Jiang, D.; Presser, V.; Augustyn, V. Pseudocapacitance: From Fundamental Understanding to High Power Energy Storage Materials. *Chem. Rev.* **2020**, *120*, 6738–6782. [[CrossRef](#)]
50. Ryabova, A.S.; Napol'skiy, F.S.; Poux, T.; Istomin, S.Y.; Bonnefont, A.; Antipin, D.M.; Baranchikov, A.Y.; Levin, E.E.; Abakumov, A.M.; Kéranguéven, G.; et al. Rationalizing the Influence of the Mn(IV)/Mn(III) Red-Ox Transition on the Electrocatalytic Activity of Manganese Oxides in the Oxygen Reduction Reaction. *Electrochim. Acta* **2016**, *187*, 161–172. [[CrossRef](#)]
51. Garcês Gonçalves, P.R.; De Abreu, H.A.; Duarte, H.A. Stability, Structural, and Electronic Properties of Hausmannite (Mn₃O₄) Surfaces and Their Interaction with Water. *J. Phys. Chem. C* **2018**, *122*, 20841–20849. [[CrossRef](#)]
52. Zhu, J.; Wu, Q.; Li, J. Review And Prospect of Mn₃O₄-Based Composite Materials For Supercapacitor Electrodes. *ChemistrySelect* **2020**, *5*, 10407–10423. [[CrossRef](#)]
53. Jang, J.H.; Oh, S.M. Complex Capacitance Analysis of Porous Carbon Electrodes for Electric Double-Layer Capacitors. *J. Electrochem. Soc.* **2004**, *151*, A571. [[CrossRef](#)]
54. Yu, P.; Zhang, X.; Chen, Y.; Ma, Y. Solution-Combustion Synthesis of ε-MnO₂ for Supercapacitors. *Mater. Lett.* **2010**, *64*, 61–64. [[CrossRef](#)]
55. Piumetti, M.; Fino, D.; Russo, N. Mesoporous Manganese Oxides Prepared by Solution Combustion Synthesis as Catalysts for the Total Oxidation of VOCs. *Appl. Catal. B Environ.* **2015**, *163*, 277–287. [[CrossRef](#)]

Disclaimer/Publisher's Note: The statements, opinions and data contained in all publications are solely those of the individual author(s) and contributor(s) and not of MDPI and/or the editor(s). MDPI and/or the editor(s) disclaim responsibility for any injury to people or property resulting from any ideas, methods, instructions or products referred to in the content.